Abe, S.; Abhir, J.; Acciari, V. A.; Agudo, I.; Aniello, T.; Ansoldi, S.; Antonelli, L. A.; Arbet-Engels, A.; Arcaro, C.; Artero, M.; Asano, K.; Babić, A.; Baquero, A.; de Almeida, U. Barres; Barrio, J. A.; Batković, I.; Baxter, J.; González, J. Becerra; Bednarek, W.; Bernardini, E.; Bernete, J.; Berti, A.; Besenrieder, J.; Bigongiari, C.; Biland, A.; Blanch, O.; Bonnoli, G.; Bošnjak; Burelli, I.; Busetto, G.; Campoy-Ordaz, A.; Carosi, A.; Carosi, R.; Carretero-Castrillo, M.; Castro-Tirado, A. J.; Ceribella, G.; Chai, Y.; Cifuentes, A.; Cikota, S.; Colombo, E.; Contreras, J. L.; Cortina, J.; Covino, S.; D'Ammando, F.; D'Amico, G.; D'Elia, V.; Da Vela, P.; Dazzi, F.; De Angelis, A.; De Lotto, B.

First characterization of the emission behavior of Mrk 421 from radio to very high-energy gamma rays with simultaneous X-ray polarization measurements

Published in:
Astronomy and Astrophysics

DOI:
10.1051/0004-6361/202347988

Published: 01/04/2024

Document Version
Publisher's PDF, also known as Version of record

A&A, 684, A127 (2024)
https://doi.org/10.1051/0004-6361/202347988

Astronomy & Astrophysics

First characterization of the emission behavior of Mrk 421 from radio to very high-energy gamma rays with simultaneous X-ray polarization measurements*

S. Abe[1], J. Abhir[2], V. A. Acciari[3], I. Agudo[4], T. Aniello[5], S. Ansoldi[6,44], L. A. Antonelli[5], A. Arbet-Engels[7,**], C. Arcaro[8], M. Artero[9], K. Asano[1], A. Babić[10], A. Baquero[11], U. Barres de Almeida[12], J. A. Barrio[11], I. Batković[8], J. Baxter[1], J. Becerra González[3], W. Bednarek[13], E. Bernardini[8], J. Bernete[14], A. Berti[7], J. Besenrieder[7], C. Bigongiari[5], A. Biland[2], O. Blanch[9], G. Bonnoli[5], Ž. Bošnjak[10], I. Burelli[6], G. Busetto[8], A. Campoy-Ordaz[15], A. Carosi[5], R. Carosi[16], M. Carretero-Castrillo[17], A. J. Castro-Tirado[4], G. Ceribella[7], Y. Chai[7], A. Cifuentes[14], S. Cikota[10], E. Colombo[3], J. L. Contreras[11], J. Cortina[14], S. Covino[5], F. D'Ammando[53], G. D'Amico[18], V. D'Elia[5], P. Da Vela[16,45], F. Dazzi[5], A. De Angelis[8], B. De Lotto[6], R. de Menezes[19], A. Del Popolo[20], J. Delgado[9,46], C. Delgado Mendez[14], F. Di Pierro[19], L. Di Venere[21], D. Dominis Prester[22], A. Donini[5], D. Dorner[2], M. Doro[8], D. Elsaesser[23], G. Emery[24], J. Escudero[4], L. Fariña[9], A. Fattorini[23], L. Foffano[5], L. Font[15], S. Fröse[23], S. Fukami[2], Y. Fukazawa[25], R. J. García López[3], M. Garczarczyk[26], S. Gasparyan[27], M. Gaug[15], J. G. Giesbrecht Paiva[12], N. Giglietto[21], F. Giordano[21], P. Gliwny[13], N. Godinović[28], T. Gradetzke[23], R. Grau[9], D. Green[7], J. G. Green[7], P. Günther[29], D. Hadasch[1], A. Hahn[7], T. Hassan[14], L. Heckmann[7,47], J. Herrera[3], D. Hrupec[30], M. Hütten[1], R. Imazawa[25], T. Inada[1], K. Ishio[13], I. Jiménez Martínez[14], J. Jormanainen[31], D. Kerszberg[9], G. W. Kluge[18,48], Y. Kobayashi[1], P. M. Kouch[31], H. Kubo[1], J. Kushida[32], M. Láinez Lezáun[11], A. Lamastra[5], F. Leone[5], E. Lindfors[31], L. Linhoff[23], S. Lombardi[5], F. Longo[6,49], R. López-Coto[4], M. López-Moya[11], A. López-Oramas[3], S. Loporchio[21], A. Lorini[33], B. Machado de Oliveira Fraga[12], P. Majumdar[34], M. Makariev[35], G. Maneva[35], N. Mang[23], M. Manganaro[22], S. Mangano[14], K. Mannheim[29], M. Mariotti[8], M. Martínez[9], M. Martínez-Chicharro[14], A. Mas-Aguilar[11], D. Mazin[1,50], S. Menchiari[33], S. Mender[23], D. Miceli[8], T. Miener[11], J. M. Miranda[33], R. Mirzoyan[7], M. Molero González[3], E. Molina[3], H. A. Mondal[34], A. Moralejo[9], D. Morcuende[11], T. Nakamori[36], C. Nanci[5], L. Nava[5], V. Neustroev[37], L. Nickel[23], M. Nievas Rosillo[3], C. Nigro[9], L. Nikolić[33], K. Nilsson[31], K. Nishijima[32], T. Njoh Ekoume[3], K. Noda[38], S. Nozaki[7], Y. Ohtani[1], A. Okumura[39], J. Otero-Santos[3], S. Paiano[5], M. Palatiello[6], D. Paneque[7,**], R. Paoletti[33], J. M. Paredes[17], D. Pavlović[22], M. Peresano[19], M. Persic[6,51], M. Pihet[8], G. Pirola[7], F. Podobnik[33], P. G. Prada Moroni[16], E. Prandini[8], G. Principe[6], C. Priyadarshi[9], W. Rhode[23], M. Ribó[17], J. Rico[9], C. Righi[5], N. Sahakyan[27], T. Saito[1], K. Satalecka[31], F. G. Saturni[5], B. Schleicher[29], K. Schmidt[23], F. Schmuckermaier[7,79,**], J. L. Schubert[23], T. Schweizer[7], A. Sciaccaluga[5], J. Sitarek[13], V. Sliusar[24], D. Sobczynska[13], A. Stamerra[5], J. Strišković[30], D. Strom[7], M. Strzys[1], Y. Suda[25], S. Suutarinen[31], H. Tajima[39], M. Takahashi[39], R. Takeishi[1], F. Tavecchio[5], P. Temnikov[35], K. Terauchi[40], T. Terzić[22], M. Teshima[7,52], L. Tosti[41], S. Truzzi[33], A. Tutone[5], S. Ubach[15], J. van Scherpenberg[7], M. Vazquez Acosta[3], S. Ventura[33], I. Viale[8], C. F. Vigorito[19], V. Vitale[42], I. Vovk[1], R. Walter[24], M. Will[7], C. Wunderlich[33], T. Yamamoto[43], I. Liodakis[54,78], S. G. Jorstad[55], L. Di Gesu[56], I. Donnarumma[56], D. E. Kim[57,58,59], A. P. Marscher[55], R. Middei[60,61], M. Perri[60,61], S. Puccetti[60], F. Verrecchia[60,61], C. Leto[56], I. De La Calle Pérez[62], E. Jiménez-Bailón[62], D. Blinov[63,64,65], I. G. Bourbah[65], S. Kiehlmann[66,65], E. Kontopodis[65], N. Mandarakas[66,65], R. Skalidis[67], A. Vervelaki[65], F. J. Aceituno[4], B. Agís-González[4], A. Sota[4], M. Sasada[68], Y. Fukazawa[69,70,71], K. S. Kawabata[69,70,71], M. Uemura[69,70,71], T. Mizuno[70], H. Akitaya[72], C. Casadio[66,65], I. Myserlis[73,74], A. Sievers[73], A. Lähteenmäki[75,76], I. Syrjärinne[75,76], M. Tornikoski[75], Q. Salomé[54,75], M. Gurwell[77], G. K. Keating[77], and R. Rao[77]

(Affiliations can be found after the references)

Received 15 September 2023 / Accepted 16 December 2023

* All data shown in Figs. 1, 2, 5, 7, and 8 are available at the CDS via anonymous ftp to cdsarc.cds.unistra.fr (130.79.128.5) or via https://cdsarc.cds.unistra.fr/viz-bin/cat/J/A+A/684/A127

** Corresponding authors: A. Arbet-Engels, F. Schmuckermaier and D. Paneque, e-mail: contact.magic@mpp.mpg.de

ABSTRACT

Aims. We have performed the first broadband study of Mrk 421 from radio to TeV gamma rays with simultaneous measurements of the X-ray polarization from IXPE.

Methods. The data were collected as part of an extensive multiwavelength campaign carried out between May and June 2022 using MAGIC, *Fermi*-LAT, *NuSTAR*, *XMM-Newton*, *Swift*, and several optical and radio telescopes to complement IXPE data.

Results. During the IXPE exposures, the measured 0.2–1 TeV flux was close to the quiescent state and ranged from 25% to 50% of the Crab Nebula without intra-night variability. Throughout the campaign, the very high-energy (VHE) and X-ray emission are positively correlated at a 4σ significance level. The IXPE measurements reveal an X-ray polarization degree that is a factor of 2–5 higher than in the optical/radio bands; that implies an energy-stratified jet in which the VHE photons are emitted co-spatially with the X-rays, in the vicinity of a shock front. The June 2022 observations exhibit a rotation of the X-ray polarization angle. Despite no simultaneous VHE coverage being available during a large fraction of the swing, the *Swift*-XRT monitoring reveals an X-ray flux increase with a clear spectral hardening. This suggests that flares in high synchrotron peaked blazars can be accompanied by a polarization angle rotation, as observed in some flat spectrum radio quasars. Finally, during the polarization angle rotation, *NuSTAR* data reveal two contiguous spectral hysteresis loops in opposite directions (clockwise and counterclockwise), implying important changes in the particle acceleration efficiency on approximately hour timescales.

Key words. radiation mechanisms: non-thermal – galaxies: active – BL Lacertae objects: individual: Mrk 421 – gamma rays: general – X-rays: galaxies

1. Introduction

Blazars are a class of jetted active galactic nuclei (AGNs) where the relativistic plasma jet is oriented at a small angle to the line of sight from Earth. They emit across the full electromagnetic spectrum, from the radio to very high-energy (VHE) gamma rays ($E > 100$ GeV). Blazars with no or very faint emission lines in the optical band are referred to as BL Lac-type objects (Urry & Padovani 1995).

The spectral energy distribution (SED) of BL Lac-type objects is dominated by the nonthermal radiation emission from the jet. The SED shows two large components, one peaking from the radio to X-rays and a second component located in the gamma rays. It is widely accepted, based on spectral and polarization characteristics, that the first component originates from synchrotron radiation produced by relativistic electrons and/or positrons in the magnetic field within the jet. The exact origin of the second component is difficult to determine and still under debate. A possible scenario is electron inverse Compton (IC) scattering on synchrotron photons making up the first component, the synchrotron self-Compton (SSC) model (Maraschi et al. 1992; Madejski et al. 1999). In some cases, an additional target photon field for IC scattering is introduced to properly describe the SED of BL Lacs (e.g., Madejski et al. 1999; Böttcher et al. 2013). Scenarios involving hadronic particles also provide possible explanations for the gamma-ray emission (Mannheim 1993; Cerruti et al. 2015). A common approach for classifying BL Lac-type objects is by the peak frequency of their synchrotron component (Urry & Padovani 1995; Padovani et al. 2017). Following the nomenclature of Abdo et al. (2010a), blazars showing a synchrotron peak frequency $\nu_s < 10^{14}$ Hz are labeled low synchrotron peaked blazars (LSPs). Intermediate synchrotron peaked blazars (ISPs) show peak frequencies of 10^{14} Hz $< \nu_s < 10^{15}$ Hz. Blazars with $\nu_s > 10^{15}$ Hz are defined as high synchrotron peaked (HSPs).

Markarian 421 (Mrk 421; RA = $11^h4'27.31''$, Dec = $38°12'31.8''$, J2000, $z = 0.031$) is an archetypal HSP and among the closest and most extensively studied extragalactic sources in the VHE sky (e.g., Horan et al. 2009; Baloković et al. 2016; Acciari et al. 2021). Nevertheless, the exact processes for the acceleration of high-energy particles and the resulting emission mechanisms in Mrk 421, and blazars generally, remain unclear. One promising approach for testing acceleration and emission scenarios in HSPs is to measure the linear polarization throughout the spectrum (Marscher & Gear 1985; Zhang & Böttcher 2013; Tavecchio 2021). Polarization measurements also provide important clues about the magnetic field ordering.

Prior blazar polarization measurements fell short of HSP synchrotron peak frequencies, extending only up to optical frequencies. Optical polarization measurements are thus not sufficient to probe the most energetic electrons freshly accelerated inside the jet. Since December 9, 2021, the Imaging X-ray Polarimetry Explorer (IXPE) has been in orbit (Weisskopf 2022) and is able to perform measurements of the linear polarization of blazars between 2 and 8 keV. The first detection of X-ray polarization from the blazar Markarian 501 (Mrk 501) by IXPE was reported in Liodakis et al. (2022). A high degree of linear polarization, at the level of 10%, was detected without significant polarization variability. The X-ray polarization was in fact found to be significantly higher than in the optical and radio bands. These properties suggest a shock acceleration model with an energy-stratified electron population. IXPE observed Mrk 421 in May and June 2022. Part of the results were published in Di Gesu et al. (2022) and Di Gesu (2023). Similarly to Mrk 501, a high degree of linear polarization was detected in the X-ray compared to the optical and radio.

Since 2009, the blazar Mrk 421 has been the focus of a multiyear program consisting of dedicated half-year observations with a number of instruments covering the broadband emission from the radio to VHE gamma rays. The first publication of this extensive observation program was Abdo et al. (2011). Triggered by the planned observations of Mrk 421 by IXPE, the multi-instrument observations related to the extensive campaign on Mrk 421 were intensified during (as well as before and after) the times when IXPE observed Mrk 421. This intensified monitoring was particularly important for the Florian Goebel Major Atmospheric Gamma Imaging Cherenkov (MAGIC). In this work we present the first observations of a blazar in VHE gamma rays accompanied by simultaneous X-ray polarization measurements. We have coordinated observations from a great number of instruments, complementing the IXPE and VHE measurements with detailed coverage in X-rays by the *Neil Gehrels Swift* Observatory (*Swift*), the X-ray Multi-Mirror Mission (*XMM-Newton),* and the Nuclear Spectroscopic Telescope Array (*NuSTAR*). High-energy gamma-ray observations are provided by the Large Area Telescope (LAT) on board the *Fermi* Gamma-ray Space Telescope (*Fermi*-LAT).

This paper is structured as follows: in Sect. 2 we describe the observations and data analysis conducted with the different instruments. In Sect. 3 we provide a detailed characterization of the multiwavelength (MWL) emission during the IXPE observations, focusing on the spectral evolution, polarization features, and intra-night variability. In Sect. 4 we investigate the MWL behavior and correlations across the full campaign, spanning from May to June 2022. Finally, in Sect. 5 we summarize and discuss the experimental findings of this study.

2. Observations and data processing

2.1. MAGIC

The MAGIC telescopes consist of two 17-meter imaging atmospheric Cherenkov telescopes, MAGIC I and MAGIC II, located at the Observatorio del Roque de los Muchachos (ORM; 28.762°N 17.890°W, 2200 m above sea level) on the Canary Island of La Palma. Stereoscopic observations have been performed since 2009, enabling the detection of gamma rays with energies from about 30 GeV up to $\gtrsim$100 TeV (Aleksić et al. 2016; MAGIC Collaboration 2020).

During the full time period covered by this work, we observed Mrk 421 for 20.2 h in total. The analysis is performed using the MAGIC Analysis and Reconstruction Software (MARS; Zanin et al. 2013; Aleksić et al. 2016), in the zenith angle range between 5° and 62°. After applying quality cuts to remove data taken at too high of a zenith angle and during adverse weather conditions, 17.3 h of data remained. The data were taken under low moonlight conditions, thus limiting contamination from night sky background light (Ahnen et al. 2017b). Thanks to the brightness and proximity of Mrk 421, two separate light curves can be obtained in the VHE regime covering an energy range from 0.2–1 TeV and above 1 TeV. The former light curve only contains data taken with a zenith angle of up to 50° due to the increasing energy threshold at larger zeniths (Aleksić et al. 2016), while the latter includes the entire zenith range.

The spectral analysis of the MAGIC data was performed by fitting the data with a log-parabolic model defined as follows:

$$\frac{\mathrm{d}N}{\mathrm{d}E} = f_0 \left(\frac{E}{E_0}\right)^{\alpha-\beta\log_{10}(E/E_0)} . \quad (1)$$

The normalization constant is given by f_0, α is the photon index at a normalization energy E_0, and β is the curvature parameter. For the normalization energy, E_0, a fixed value of 300 GeV was chosen. Flux points were obtained by performing the Tikhonov unfolding procedure as described in Albert et al. (2007). All obtained parameters and flux points were corrected for the extragalactic background light absorption following the model of Domínguez et al. (2011).

2.2. Fermi-LAT

The LAT instrument is a pair-conversion telescope on board the *Fermi* satellite (Atwood et al. 2009; Ackermann et al. 2012) surveying the gamma-ray sky in the 20 MeV to >300 GeV energy range. For this work, we performed an unbinned-likelihood analysis using tools from the `FERMITOOLS` software[1] v2.0.8. We used the instrument response function `P8R3_SOURCE_V2` and the diffuse background models[2] `gll_iem_v07` and `iso_P8R3_SOURCE_V3_v1`.

We selected `Source` class events between 0.3 GeV and 300 GeV in a circular region of interest (ROI) with a radius of 20° around Mrk 421. The events with a zenith angle >90° were discarded to limit the contribution from limb gamma rays. To build the source model, we included all sources from the fourth *Fermi*-LAT source catalog Data Release 2 (4FGL-DR2; Abdollahi et al. 2020; Ballet et al. 2020) that are found within the ROI plus an annulus of 5°. Mrk 421 was modeled with a simple power-law function. In order to build light curves, the source model was fitted to the data by letting free to vary the normalization and the spectral parameters of all sources within 7° of the target. Above 7°, all spectral parameters were fixed to the 4FGL-DR2 values. The normalizations of the diffuse background components were left as free parameters. When the fit did not converge, the model parameters were fixed to the 4FGL-DR2 values for sources detected with a test statistic (TS; Mattox et al. 1996) below 4. If after that the fit still did not converge, we gradually increased the TS threshold below which the model parameters are fixed, until convergence is achieved.

We produced a light curve in the 0.3–300 GeV[3] band using 3-day time bins. In all time bins, the source is detected with TS > 25 (i.e., >5σ). Finally, we computed a SED around each IXPE observation by averaging the data over 7 days. This time bin choice is a good compromise solution, given the flux variability observed in the light curves, and the limited sensitivity of LAT to measure gamma-ray spectra over short time intervals.

2.3. NuSTAR

This work comprises two multi-hour exposures from the Nuclear Spectroscopic Telescope Array (*NuSTAR;* Harrison et al. 2013), which consists of two co-aligned X-ray telescopes focusing on two independent focal plane modules, FPMA and FPMB. The instrument provides unprecedented sensitivity in the 3–79 keV band. The observations took place June 4-5, 2022 (MJD 59734 to MJD 59735) and June 7–8, 2022 (MJD 59737 to MJD 59738; observation ID 60702061002 and 60702061004, respectively), with a total exposure time of 21 ksec and 23 ksec, respectively. The raw data were processed using the *NuSTAR* Data Analysis Software (NuSTARDAS) package v.2.1.1 and CALDB version 20220912. The events were screened in the `nupipeline` process with the flags `tentacle=yes` and `saamode=optimized` in order to remove any potential background increase caused by the South Atlantic Anomaly passages. The source counts were obtained from a circular region centered around Mrk 421 with a radius of ≈140″. The background events were extracted from a source-free nearby circular region having the same radius. The spectra were then grouped with the `grppha` task to obtain at least 20 counts in each energy bin.

For both exposures, the source spectra dominate over the background up to roughly ≈30 keV. Hence, in this work we decided to quote fluxes only up to 30 keV, and in two separate energy bands: 3–7 keV and 7–30 keV. The best-fit spectral parameters averaged over the respective observations were obtained in the full *NuSTAR* bandpass, 3–79 keV. We fitted the spectra using `XSPEC` (Arnaud 1996) assuming a log-parabolic function with a normalization energy fixed to 1 keV. A simple power-law model provides a significantly worse description of the spectra (at a level >5σ based on the χ^2) and a curvature is detected during both observations. Here, and for the rest of the X-ray analysis performed in this work, a photoelectric absorption component was added to the model assuming an equivalent hydrogen column density fixed to $N_{\rm H} = 1.34 \times 10^{20}\,\mathrm{cm}^{-2}$ (HI4PI Collaboration 2016). The fluxes and spectral parameters were computed by fitting simultaneously FPMA and FPMB. The cross-calibration factor between the two focal plane modules is

[1] https://fermi.gsfc.nasa.gov/ssc/data/analysis/
[2] http://fermi.gsfc.nasa.gov/ssc/data/access/lat/\BackgroundModels.html

[3] The threshold energy of 0.3 GeV was preferred over the usual 0.1 GeV in order to exploit the improved angular resolution of *Fermi*-LAT at higher energies. A higher energy threshold also reduces background contamination, which leads to an overall improvement of the signal-to-noise ratio for hard sources such as Mrk 421 (photon index > −2).

for all bins within 0.95 and 1.05, thus well inside the expected systematics (Madsen et al. 2015).

2.4. Swift-XRT

We organized several X-ray pointings from the *Swift* X-ray Telescope (XRT; Burrows et al. 2005). A special effort was put to schedule the observations simultaneously to the MAGIC exposures. The *Swift*-XRT observations were performed in both Windowed Timing (WT) and Photon Counting (PC) readout modes. We processed the data using the XRTDAS software package (v.3.7.0) developed by the ASI Space Science Data Center[4] (SSDC), released by the NASA High Energy Astrophysics Archive Research Center (HEASARC) in the HEASoft package (v.6.30.1). In order to calibrate and clean the events, data were reprocessed with the `xrtpipeline` script and using calibration files from *Swift*-XRT CALDB (version 20210915) within the `xrtpipeline`.

For each observation, the X-ray spectrum was extracted from the calibrated and cleaned event file. In both WT and PC modes, the events were selected within a circle of 20-pixel (∼47 arcsec) radius. The background was then extracted from a nearby, source-free, circular region with a 40-pixel radius. The ancillary response files (ARF) were generated with the `xrtmkarf` task applying corrections for point spread function losses and charge coupled device (CCD) defects using the cumulative exposure map.

The 0.3−10 keV source spectra were binned using the `grppha` task by requiring at least 20 counts per energy bin. We then used `XSPEC` using both a power-law and log-parabola models (with a pivot energy fixed at 1 keV). In the vast majority of the observations, the statistical preference for a log-parabola model is significant (>5σ). The fluxes were extracted in the 0.3–2 keV, and 2–10 keV energy bands.

2.5. XMM-Newton

The *XMM-Newton* observatory carries on board several co-aligned X-ray instruments: the European Photon Imaging Camera (EPIC) and two reflection grating spectrometers (RGS1 and RGS2; Jansen et al. 2001). The EPIC cameras consist of two metal oxide semiconductors (EPIC-MOS1 and MOS2; Turner et al. 2001) and one pn junction (EPIC-pn, Strüder et al. 2001) CCD arrays operating in the 0.2–10 keV energy band. All *XMM-Newton* observations presented in this paper were taken with the EPIC camera under TIMING mode with the THICK filter. Data are available in the EPIC-pn and EPIC-MOS2 cameras. Observing times per observation range between ∼17 ksec and ∼47 ksec. Our sample was analyzed using the *XMM-Newton* standard Science Analysis System (SAS; v20.0.0; Gabriel et al. 2004) and most updated calibration files. Event lists were produced for the two EPIC cameras following the standard SAS reduction procedure. Periods of high-background activity were removed following the standard method (Lumb et al. 2002).

The source and background regions for the EPIC-pn and EPIC-MOS2 cameras were extracted following the same method as described in de la Calle Pérez et al. (2021). We extracted spectra in the full energy range (0.2–10 keV) with an energy resolution of 5 eV. The spectra were re-binned to avoid over sampling the intrinsic energy resolution of the EPIC cameras by a factor larger than 3, while making sure that each spectral channel contains at least 25 background-subtracted counts. Spectral fits were performed with the `XSPEC` package (Arnaud 1996) in the energy range 0.6–10 keV (a minimum fit energy of ≈0.6 keV is recommended by the official SAS documentation[5] for TIMING mode observations to avoid low energy noise distorting the spectra). For every observation, we performed spectral fits and derived spectral parameters from the combined EPIC instruments available (i.e., EPIC-pn and EPIC-MOS2). All spectra were fitted using a log-parabola model (with a pivot energy set at 1 keV).

The most updated comparison of X-ray satellite observations shows that EPIC-pn data slightly differ from the *NuSTAR* and *Swift* data both in flux and slope (Madsen et al. 2017). The EPIC-pn fluxes are significantly lower than the *NuSTAR* fluxes, typically by the order of 20%. Although, based on the analysis performed so far, it is not possible to elucidate which instrument recovers the correct X-ray fluxes, the *XMM-Newton* Science Operation Center has proposed a correction to the *XMM-Newton* EPIC data that can be applied for observations performed simultaneously with *NuSTAR*. This correction has been applied to all the EPIC data that has simultaneous data with *NuSTAR*. The correction was applied in the ARF generation and can be done using the standard SAS task `arfgen` including the parameter `applyabsfluxcorr=yes`.[6]

2.6. IXPE

The IXPE telescope (Weisskopf 2022) is the first instrument capable of resolving the X-ray polarization degree and angle in blazars. Here, we exploited the first three IXPE observations of Mrk 421, which took place in the first half of 2022 and were accompanied by the simultaneous MAGIC monitoring. The first observation spanned from May 4, 2022 10:00 UTC (MJD 59703) until May 6, 2022 11:10 UTC (MJD 59705), for a total exposure of 97 ksec. The two additional observations took place in June 2022: from June 4, 2022 10:56 UTC until June 6, 2022 11:08 UTC (MJD 59734 to MJD 59736; 96 ksec exposure time), and from June 7, 2022 08:49 UTC until June 9, 2022 09:51 UTC (MJD 59737 to MJD 59739; 86 ksec exposure time). All results shown in this paper were taken from Di Gesu et al. (2022, May observation) and Di Gesu (2023, June observations). We refer the reader to these two works for details about the analysis procedure.

During the first IXPE observation, in May 2022, no variability of the polarization degree and angle is measured (Di Gesu et al. 2022), and the values averaged over the full exposure are considered. Regarding the two observations in June 2022, the polarization angle exhibits a large rotation (Di Gesu 2023) at a speed of 80 ± 9°/day (June 4–6, 2022; MJD 59734 to MJD 59736) and 91 ± 8°/day (June 7–9, 2022; MJD 59737 to MJD 59739). The rotation is evident when considering the data binned in 3 h intervals. Based on simulations, Di Gesu (2023) estimated that the probability of detecting these rotations due to random walks is about 2%, and thus, it is highly unlikely to have occurred by chance. As described in Di Gesu (2023), the polarization degree remains consistent with a constant behavior hypothesis.

[4] https://www.ssdc.asi.it/

[5] https://www.cosmos.esa.int/web/xmm-newton/calibration-documentation

[6] https://xmmweb.esac.esa.int/docs/documents/CAL-TN-0230-1-3.pdf

2.7. Swift-UVOT

We obtained a coverage in the UV band from the *Swift* UV/Optical Telescope (UVOT; Roming et al. 2005). We considered observations between April 26, 2022 (MJD 59695) and June 27, 2022 (MJD 59757) with the $W1, M2$ and $W2$ filters. We selected a sample of 43 observations of Mrk 421 from the official data archive, by applying standard quality checks to all observations in the chosen time interval, excluding those with unstable attitude or affected by contamination from a nearby star light (51 UMa). For each observation, we performed photometry over the total exposures in each filter. The same apertures for source counts (the standard with 5 arcsec radius) and background estimation (mostly three-four circles of ∼16 arcsec radii off the source) were applied to all. We used the official software included in the HEASoft 6.23 package, from HEASARC, to perform the photometry extraction and then applied the official calibrations (Breeveld et al. 2011) included in the recent CALDB release (20201026). Finally, we de-reddened source fluxes according to a mean interstellar extinction curve (Fitzpatrick 1999) and the mean Galactic $E(B-V)$ value of 0.0123 mag (Schlegel et al. 1998; Schlafly & Finkbeiner 2011).

2.8. Optical observations

In the optical, we exploited R-band photometric and polarimetric observations from the RoboPol (Skinakas Observatory, Greece; King et al. 2014; Ramaprakash et al. 2019), Nordic Optical Telescope (NOT; ORM, Spain), and KANATA (Higashi-Hiroshima observatory, Japan) telescopes. We also made use of H-band (infrared; IR) data from the Perkins telescope (Perkins Telescope Observatory, Flagstaff, AZ). All these data were published in Di Gesu et al. (2022) and Di Gesu (2023), where more details on the analysis procedures can be found. Additional polarimetric and photometric observations of the source in the Johnson Cousins R band were performed at Sierra Nevada Observatory, Granada, Spain, with a four-unit polarized filter-wheel mounted at the 0.9 m telescope (here after dubbed T90). Unpolarized standard stars were also observed to compute the instrumental polarization that was subtracted from the actual data. Standard pre-reduction and analysis steps were performed.

All the polarization and photometric data were corrected for the contribution of the host galaxy using the host fluxes reported in Nilsson et al. (2007). The intrinsic polarization degree was obtained using the following formula: $P_{\rm deg,intr} = P_{\rm deg,obs} \cdot I/(I - I_{\rm host})$, where $P_{\rm deg,obs}$ the observed polarization degree, I the observed flux and $I_{\rm host}$ the host flux. Finally, the flux densities were also corrected for a galactic extinction of 0.033 mag according to the NASA/IPAC Extragalactic Database (NED).[7]

2.9. Radio observations

We collected data in the microwave band at 3.5 mm (86.24 GHz) and 1.3 mm (230 GHz) wavelengths with the 30 m telescope of the Institut de Radioastronomie Millimetrique (IRAM) that is located at the Pico Veleta Observatory (Sierra Nevada, Granada, Spain). The observations were performed within the Polarimetric Monitoring of AGN at Millimeter Wavelengths (POLAMI) program[8] (Agudo et al. 2018a,b). The four Stokes parameters (I, Q, U, and V) were recorded simultaneously using the XPOL procedure (Thum et al. 2008). The data reduction and calibration was achieved following the POLAMI procedure described in Agudo et al. (2018a).

Additional radio observations were performed by the Metsähovi telescope. A detailed description of the data reduction and analysis can be found in Teraesranta et al. (1998). In short, observations at 37 GHz are conducted using the 13.7 m Metsähovi telescope. Under optimal conditions the detection limit of the telescope at 37 GHz is approximately 0.2 Jy. For the flux density, DR 21 is used as the primary calibrator, and NGC 7027, 3C 274, and 3C 84 are used as secondary calibrators. The flux density errors include the uncertainty in the absolute flux calibration as well as the root mean square of the measurement. We considered as detections only the observations with a signal-to-noise ratio greater than four.

Finally, we collected millimeter radio polarimetric measurements at 1.3 mm (approximately 230 GHz) with the Submillimeter Array (SMA; Ho et al. 2004). The observations were conducted within the SMA Monitoring of AGNs with POLarization (SMAPOL) program in full polarization mode using SMA polarimeter (Marrone & Rao 2008) and SWARM correlator (Primiani et al. 2016). The polarized intensity, position angle, and polarization percentage were derived from the Stokes I, Q, and U visibilities and calibrated with the MIR software package[9] using MWC 349 A, Callisto (total flux calibrators), and 3C 286 (polarized calibrator).

3. Characterization of the VHE to radio behavior during IXPE observations

Figure 1 shows the MWL light curves from MJD 59695 (April 26, 2022) to MJD 59760 (June 30, 2022), which encompasses all IXPE observing periods. In the top row, the VHE energy bands (0.2–1 TeV and >1 TeV) are shown. As previously mentioned, data observed at a zenith above 50° were excluded from the 0.2–1 TeV energy band, while for the >1 TeV fluxes no cut on the zenith distance was applied. The cut on the zenith distance is necessary because the energy threshold increases to above 0.2 TeV for zenith angles greater than 50°, and hence we would introduce artificial downward fluctuations in the reported fluxes (e.g., by producing a light curve above 0.2 TeV when using data with an energy threshold well above this energy). In any case, this selection cut only removed a small fraction of the data from the 0.2–1 TeV light curve (it affects only three nights, removing a total of ≈2 h), and no intra-night variability was found in any of the two bands. Thus, the slightly different underlying data selection does not affect in any significant manner the hardness ratio. Measurements from *Fermi*-LAT in the 0.3–300 GeV band are portrayed in the second panel from the top. The *Fermi*-LAT fluxes are computed in 3-day bins, providing a good trade-off between flux uncertainty and temporal resolution. In X-rays, third panel, a dense temporal coverage is given by *Swift*-XRT in two energy bands (0.3–2 keV and 2–10 keV). On selected days during the IXPE observations, additional data by *NuSTAR* and *XMM-Newton* are available. We quantified the corresponding spectral evolution using the hardness ratio in X-rays, defined as the ratio of the 2−10 keV flux to the 0.3−2 keV flux, in the fourth panel. Additionally, the hardness ratio of the VHE data (defined as the ratio of the >1 TeV flux to the 0.2−1 TeV flux) is shown. UV observations from *Swift*-UVOT in the $W1, M2$ and $W2$ filters are shown in the fifth panel from the top. We complement the MWL light curves with further data in the optical/IR and radio,

[7] https://ned.ipac.caltech.edu/
[8] https://polami.iaa.es/
[9] https://lweb.cfa.harvard.edu/~cqi/mircook.html

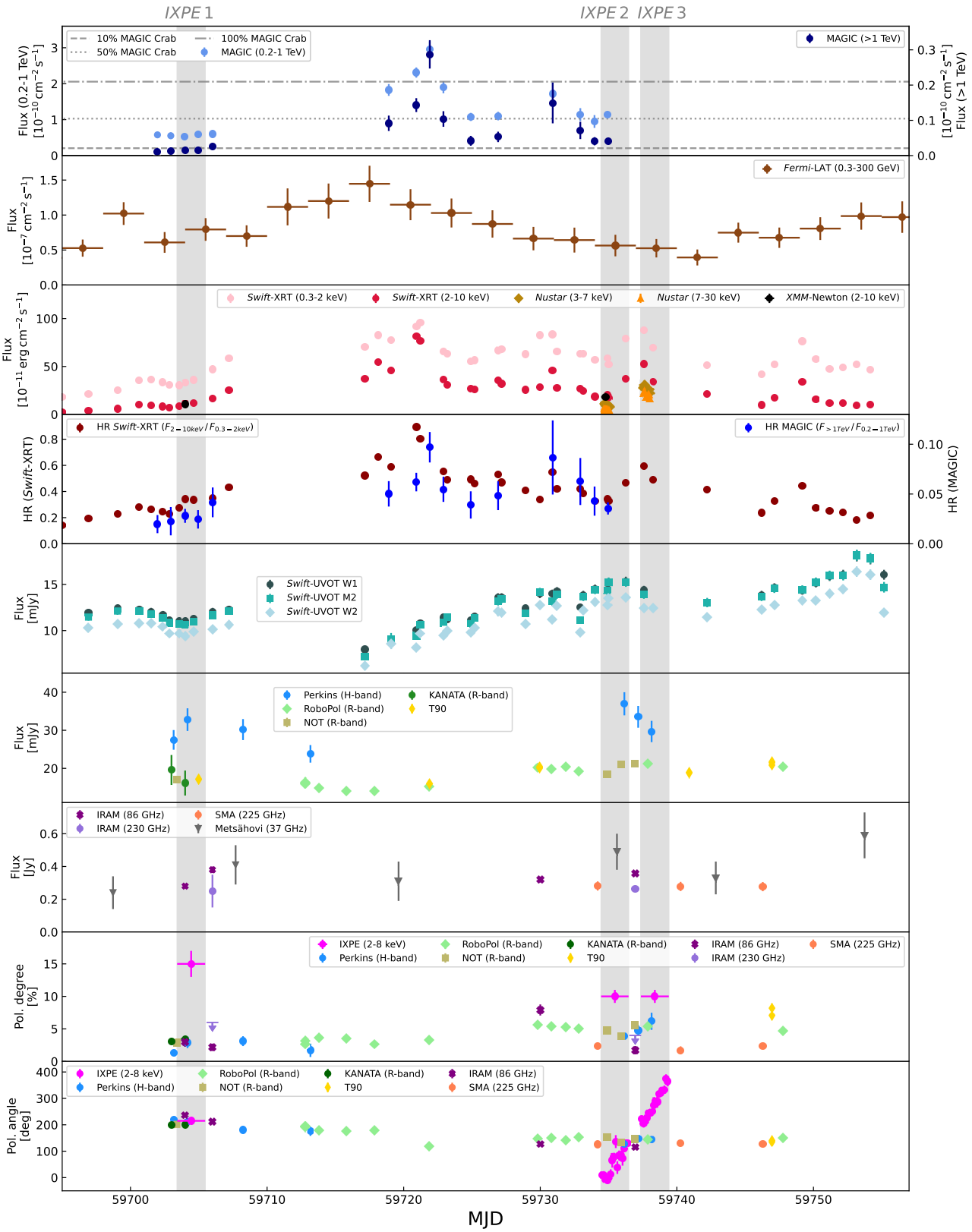

Fig. 1. MWL light curve for Mrk 421 covering the whole campaign from MJD 59695 (April 26, 2022) to MJD 59757 (June 27, 2022). The gray bands correspond to the three IXPE observations. Top to bottom: MAGIC fluxes in daily bins for two energy bands (note the two different *y*-axes); *Fermi*-LAT fluxes in 3 day bins; X-ray fluxes in daily bins including *Swift*-XRT, *NuSTAR* and IXPE; hardness ratio between the high- and low-energy fluxes of *Swift*-XRT and between the two VHE bands of MAGIC (note the two different *y*-axes); optical *R*-band data from NOT, RoboPol KANATA; IR *H*-band data from Perkins; radio data from IRAM and polarization degree and polarization angle observations in the optical to radio from NOT, RoboPol, KANATA, Perkins, IRAM, SMA and in X-rays from IXPE.

which are plotted in the sixth and seventh panel, respectively. The last two panels at the bottom of Fig. 1 display the evolution of the polarization degree and polarization angle in the radio, optical, IR and X-ray.

3.1. IXPE observation in May 2022

The first observation of Mrk 421 by IXPE occurred between May 4 and May 6, 2022 (MJD 59703.42–MJD 59705.47) and is shown as the first gray band in Fig. 1. Here and in the following, this epoch will be referred to as IXPE 1.

The MAGIC telescopes achieved a continuous daily coverage over the entire IXPE exposure. In both VHE energy bands, the flux exhibits a constant behavior throughout the specified time period, showing a flux slightly below 10% of the emission of the Crab Nebula[10] in the range above 1 TeV, and around 25% for the 0.2–1 TeV range. We do not find significant flux or spectral variability on daily and sub-daily timescales. A simultaneous X-ray characterization is obtained thanks to *Swift*-XRT as well as a long exposure from *XMM-Newton* on MJD 59704 (May 5, 2022). The flux in both energy bands of the *Swift*-XRT instrument exhibits moderate daily variability. In the 0.3–2 keV band, a flux increase at the level of 20% is observed, while it is 40% in the 2–10 keV band. The hardness ratio rises from 0.23 ± 0.01 up to almost 0.35 ± 0.01, indicating a harder-when-brighter trend in agreement with previous observations of Mrk 421 (see for instance Aleksić et al. 2015a; Acciari et al. 2021; MAGIC Collaboration 2021). Regarding the multi-hour *XMM-Newton* pointing, the average 2–10 keV flux (pink marker in Fig. 1) is consistent with *Swift*-XRT results. During the observation, little variability is observed. A 500 s binned *XMM-Newton* light curve is shown in Fig. A.1. The concurrent optical/IR (*R* band and *H* band) and radio flux data in Fig. 1 around IXPE 1 show small variability although the limited temporal coverage prevents a detailed variability characterization.

The degree of polarization from radio to optical shows slightly fluctuating values around 3%. The results of the IXPE observation (taken from Di Gesu et al. 2022) show a much higher constant degree of polarization of 15 ± 2 % in the X-ray band. The polarization angle determined by IXPE is $215 \pm 4°$ (or $35 \pm 4°$, if one considers the 180° ambiguity in polarization angle measurements) and is in agreement with the angles measured in radio to optical, which range from around 200° up to 230° and also remains constant throughout the observation period.

3.2. IXPE observation in June 2022

The second and third IXPE observations of Mrk 421 were performed between June 4 and 6, 2022 (MJD 59734.46–MJD 59736.46) and between June 7 and 9, 2022 (MJD 59737.36–MJD 59739.41). In the following, these two observing epochs are dubbed IXPE 2 and IXPE 3, respectively. They are highlighted with vertical gray bands in Fig. 1.

MAGIC could only observe during the first day of the IXPE 2 period as well as two days before, for a total of 3.3 h of observation. Over the course of three days, the flux in the 0.2–1 TeV band is close to ≈50% of the Crab Nebula and ≈20% above 1 TeV, indicating about twice as much flux as during IXPE 1.

In X-rays, a significantly higher activity is also observed throughout the entire IXPE 2 and IXPE 3 windows with respect to IXPE 1, and the source exhibits clear spectral and flux variability. Between the IXPE 2 epoch and the start of the IXPE 3 epoch, the 2–10 keV flux shows a steady increase by a factor of ≈2.6, together with a clear hardening of the emission that is highlighted by the hardness ratio evolution (a more detailed spectral analysis is presented in Sect. 3.3). The peak activity in the 2–10 keV band is about five times the average flux level observed during IXPE 1. Although this flux state is still below previous X-ray outbursts of Mrk 421 (see for instance the March 2010 flare reported in Aleksić et al. 2015b), this activity is among the highest states recorded during 2022. The flux then decreases during the last *Swift*-XRT observation simultaneous to IXPE 3. The *XMM-Newton* analysis confirms the higher X-ray activity compared to IXPE 1. The observation took place at the beginning of the IXPE 2 epoch, slightly before the clear flux increase witnessed by *Swift*-XRT. In addition to *Swift*-XRT and *XMM-Newton*, a precise hard X-ray characterization was obtained thanks to two multi-hour *NuSTAR* exposures during both IXPE 2 and IXPE 3. In the third panel from the top of Fig. 1, we show the *NuSTAR* fluxes in the 3–7 keV and 7–30 keV bands using 1 h time bins. For IXPE 2, the *NuSTAR* observation was simultaneous to MAGIC. The corresponding intra-night VHE versus X-ray correlation is investigated in Sect. 3.5. During both *NuSTAR* pointings, a moderate flux change is observed on hour timescales (at the level of 30%). Nonetheless, a detailed study unveils spectral hysteresis patterns. This analysis is presented in Sect. 3.6.

Regarding the MeV-GeV band, the *Fermi*-LAT analysis shows a similar flux state as during IXPE 1, and is close to the average activity for Mrk 421 (Abdo et al. 2011). For the UV, optical, IR, and radio emission, the emission does not reveal significant evolution with respect to IXPE 1 either.

The bottom panels of Fig. 1 show the evolution of the polarization degree and angle in the X-ray 2–8 keV band (pink markers; the data are taken from Di Gesu 2023). During IXPE 2 and IXPE 3, the averaged degree is 10 ± 1%. While the polarization degree is consistent with a constant behavior (see also Sect. 3.6), the polarization angle exhibits an evident rotation, which seems continuous between the two IXPE 2 and IXPE 3 epochs. During IXPE 2, the angle rotates at an average angular velocity of $80 \pm 9°$/day amounting to a total rotation of 120°. The rotation continued at a compatible rate of $91 \pm 8°$/day during IXPE 3, for a total rotation of 140°. The significant X-ray flux increase and spectral hardening measured by *Swift*-XRT is thus accompanied by a rotation of the polarization angle. In Sect. 3.6, we investigate the short timescale spectral variability in the hard X-rays during the polarization angle rotation using simultaneous *NuSTAR* data.

It is interesting to note that at lower frequencies, in the radio, IR and optical bands, neither the flux nor polarization properties show any prominent variability. The polarization degree in the optical and IR fluctuates around 5% while the radio polarization is slightly lower, around 2% both for the 86 GHz and 230 GHz bands.

3.3. Spectral evolution throughout the IXPE observing epochs

Figure 2 presents the simultaneous broadband SEDs during each of the IXPE periods from the IR up to VHE gamma rays. In comparison, the average state of Mrk 421 taken from Abdo et al. (2011) is plotted in light gray. Since the VHE flux level reported

[10] The flux of the Crab Nebula used in this work is taken from Aleksić et al. (2016).

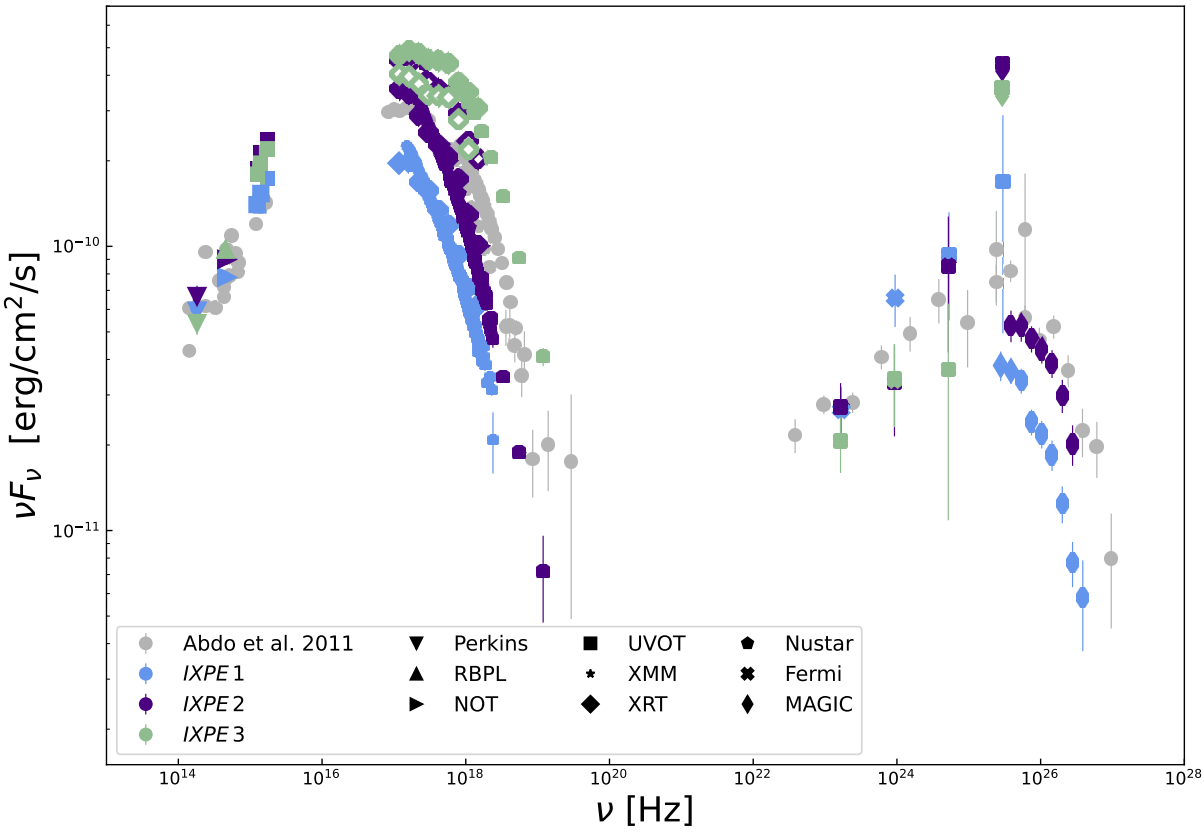

Fig. 2. Broadband SED around the three IXPE observations. Data from MAGIC were corrected for the extragalactic background light absorption using the model outlined in Domínguez et al. (2011). In plain colored markers, the *Swift*-XRT data correspond to the pointing that happened first within the IXPE windows. The *Swift*-XRT data in diamond markers with a face color in white are from the subsequent observation. For comparison, the SED of an average emission state of Mrk 421 from Abdo et al. (2011) is shown in light gray.

in Abdo et al. (2011) is close to the average state found by Whipple over a time span of 14 years (45% of the Crab Nebula flux, Acciari et al. 2014), we considered the broadband SED of Abdo et al. (2011) as an average activity state and used it as a reference for comparison. MAGIC VHE flux points from IXPE 1 were obtained by averaging all data within the corresponding IXPE exposures since we find no significant spectral no flux variability. Regarding IXPE 2, a single MAGIC observation is available and it took place at the beginning of the IXPE window, while IXPE 3 is lacking VHE coverage (see Fig. 1 and previous section). The *Fermi*-LAT SEDs were averaged over 7 days, centered around the IXPE windows. In X-rays, for IXPE 1, we show the *Swift*-XRT SED on MJD 59704.02 (May 5, 2022), which is close to the center of the IXPE window and simultaneous to the *XMM-Newton* observation. Regarding IXPE 2 and IXPE 3, we plot for each epoch the *Swift*-XRT SEDs that were first recorded within the IXPE windows. These SEDs are also accompanied by simultaneous *XMM-Newton* (for IXPE 2 only) and *NuSTAR* data (for both IXPE 2 and IXPE 3). We add *Swift*-XRT SEDs corresponding to the last pointing before the end of the IXPE windows in order to illustrate the daily timescale variability along the IXPE exposure. For the optical and IR data, we used measurements that are the closest in time to each of the X-ray observations.

Compared to the average state of Abdo et al. (2011), the IXPE 1 epoch (blue markers) displays a VHE and X-ray emission that is significantly lower. The X-ray SED is also softer, indicating a shift of the synchrotron peak toward lower frequencies. Based on a log-parabola fit in the SED space ($\nu F_\nu \propto 10^{-b(\log(\nu/\nu_p))^2}$), we derived a peak frequency located at $\nu_p = (2.00 \pm 0.07) \times 10^{16}$ Hz, while the state from Abdo et al. (2011) suggests $\nu_p \approx 10^{17}$ Hz. Throughout the IXPE 2 and IXPE 3, Fig. 2 highlights clearly the spectral changes occurring during the polarization angle swing reported by IXPE. At the beginning of IXPE 2 (plain violet color markers), the emission is roughly comparable to the typical state at all frequencies. Compared to IXPE 1, the synchrotron peak frequency increases marginally to $\nu_p = (2.27 \pm 0.09) \times 10^{16}$ Hz. The emission increases significantly during the subsequent X-ray SED, which shows a flux well above the typical state as well as an harder emission. The maximum observed brightness is reached at the start of IXPE 3 (green markers), which coincides with the second *NuSTAR* observation and shows an enhanced emission state throughout the full synchrotron peak accompanied by a significant shift of the synchrotron peak toward a higher frequency ($\nu_p = (7.6 \pm 1.3) \times 10^{16}$ Hz). A decrease is then observed the following day (shown with a white marker).

Owing to the dependence of the peak frequencies on the adopted fitting function, we also determined the synchrotron peak frequency following the phenomenological description of Ghisellini et al. (2017). We obtained values of ν_p higher by a factor of 2–3 compared to the log-parabola fit. Since the peak is not well covered for IXPE 1 and IXPE 2, and rather flat for IXPE 3, these model-dependent differences are expected. The clear trend of a synchrotron peak shifting toward higher values for IXPE 3 is still present.

Table 1. Spectral parameters from the VHE and X-ray observations around the three IXPE observing epochs.

		IXPE 1			IXPE 2			IXPE 3	
MAGIC	MJD	59703.5 to 59705.5			59734.5 to 59735.5			–	
	Flux	0.34 ± 0.01			0.67 ± 0.03			–	
	α	-2.64 ± 0.06			-2.30 ± 0.08			–	
	χ^2/d.o.f.	25.0/13			2.5/9			–	
Swift-XRT	MJD	59703.55	59704.02	59704.62	59734.92	59735.00	59736.27	59737.58	59738.25
	Flux	$0.84^{+0.04}_{-0.03}$	$1.13^{+0.04}_{-0.04}$	$1.20^{+0.04}_{-0.04}$	$2.01^{+0.05}_{-0.05}$	$1.70^{+0.05}_{-0.05}$	$3.68^{+0.08}_{-0.08}$	$5.26^{+0.05}_{-0.06}$	$3.40^{+0.12}_{-0.12}$
	α	$-2.52^{+0.02}_{-0.02}$	$-2.38^{+0.02}_{-0.02}$	$-2.38^{+0.02}_{-0.02}$	$-2.40^{+0.01}_{-0.01}$	$-2.43^{+0.02}_{-0.02}$	$-2.22^{+0.01}_{-0.01}$	$-2.07^{+0.01}_{-0.01}$	$-2.19^{+0.02}_{-0.02}$
	χ^2/d.o.f.	223.5/197	236.1/216	225.4/220	261.5/266	241.9/223	346.3/309	549.0/481	218.6/199
XMM-Newton	MJD	59703.93 to 59704.13			59734.68 to 59735.11			–	
	Flux	$1.056^{+0.002}_{-0.002}$			$1.838^{+0.002}_{-0.002}$			–	
	α	$-2.541^{+0.001}_{-0.001}$			$-2.545^{+0.001}_{-0.001}$			–	
	χ^2/d.o.f.	814.8/329			2082.13/345			–	
NuSTAR	MJD	–			59734.65 to 59735.11			59737.53 to 59738.04	
	Flux	–			0.968 ± 0.004			2.693 ± 0.006	
	α	–			-2.309 ± 0.007			-1.913 ± 0.004	
	χ^2/d.o.f.	–			704.7/761			1143.8/1133	

Notes. The table contains four primary rows corresponding to the different instruments. The first subrow for an individual instrument shows the MJD of the observations performed during the three IXPE observations given by the main columns. The second subrow contains the obtained fluxes in units of 10^{-10} erg cm^{-2} s^{-1} (for MAGIC the integrated photon flux between 200 GeV and 1 TeV is used, for *Swift*-XRT and *XMM-Newton* the flux between 2–10 keV and for *NuSTAR* the 3–7 keV flux). The spectral index α, assuming a log-parabola for MAGIC (with β fixed to 0.50 and reference energy of 300 GeV) as well as for *Swift*-XRT (with β fixed to 0.29 and reference energy of 1 keV), *XMM-Newton* (with β fixed to 0.20 and reference energy of 1 keV), and *NuSTAR* (with β fixed to 0.45 and reference energy of 1 keV) is given in the third subrow. The last subrow gives the χ^2/d.o.f. Regarding *XMM-Newton* and *NuSTAR*, the parameters were obtained by fitting jointly the data from the available cameras on board these observatories (i.e., EPIC-pn and EPIC-MOS2 for *XMM-Newton*, FPMA and FPMB for *NuSTAR*).

The obtained spectral parameters in X-rays and VHE gamma rays are listed in Table 1. As for Fig. 2, the MAGIC spectral fits are performed after averaging all nights within the IXPE windows. For all IXPE epochs, the MAGIC data show a preference for a log-parabola model (see Eq. (1)) over a simple power-law function. The preference is above 3σ for IXPE 1 and at the level of 2σ for IXPE 2. We do not observe significant variability of the curvature parameter β, which stays consistent with $\beta = 0.50$. Thus, throughout this work, the MAGIC spectra simultaneous to the IXPE observations were fitted using a log-parabola model using a fixed curvature $\beta = 0.50$. This choice removes any correlation between α and β (see Eq. (1)), providing a better assessment of the hardness evolution during the different epochs. The normalization energy was fixed to 300 GeV. The resulting best fit spectral indices of MAGIC are shown in the first primary row of Table 1.

The *Swift*-XRT spectra show a significant preference for a log-parabola model over a power law. As in the MAGIC spectral study, the data were fitted using a log-parabola with fixed curvature in order to obtain a better characterization of the hardness evolution throughout the IXPE epochs. We used here $\beta = 0.29$, which is the average curvature over the campaign. The second primary row of Table 1 presents the best fit parameters for each exposure simultaneous to IXPE (the pivot energy of the log-parabola model is 1 keV).

Regarding *XMM-Newton* and *NuSTAR*, the spectral parameters are derived in the 0.6–10 keV and 3–79 keV bands, respectively. Similarly to the fits for MAGIC and *Swift*-XRT, we fixed the curvature in the log-parabola model to $\beta = 0.2$ for *XMM-Newton* and to $\beta = 0.45$ for *NuSTAR*. For both instruments, the pivot energy was set to 1 keV.

Overall, the spectral evolution is consistent with the typical harder-when-brighter trend found frequently in Mrk 421 (Acciari et al. 2021; MAGIC Collaboration 2021). At VHE, α during IXPE 2 is smaller compared to IXPE 1 ($\alpha = -2.30 \pm 0.08$ versus $\alpha = -2.64 \pm 0.06$ for IXPE 1), while the emitted flux doubled. A similar behavior is found in X-rays with *Swift*-XRT, *XMM-Newton* and *NuSTAR* data and confirmed by the visual trend in Fig. 2. The spectral hardening is particularly evident between IXPE 2 and IXPE 3 when the X-ray polarization angle rotates. Both in *Swift*-XRT and *NuSTAR* the spectral parameter α hardens by $\approx$0.3–0.4 (see Table 1).

Most of the spectral variability in X-rays occurs on an approximately daily timescale. The shorter timescales variability can be probed thanks to the multi-hour exposures from *XMM-Newton* and *NuSTAR*. Figures A.1 and A.2 show the 0.3–2 keV the 2–10 keV fluxes (binned in 500 s) as well as the hardness ratio obtained during the observations of *XMM-Newton*. The ratios do not reveal any prominent spectral evolution over approximately hour timescales for either day. The *NuSTAR* analysis, however, reveals a moderate spectral change on approximately hour timescales, although spectral hysteresis behavior is apparent. A more detailed analysis is presented in Sect. 3.6.

3.4. Broadband evolution of the polarization degree between the IXPE epochs

Figure 3 summarizes the polarization degree as a function of the frequency for all IXPE observing epochs. The bottom panel shows the ratio to the X-ray polarization degree. For the optical and IR, we performed a weighted average of the measurements within the IXPE observing windows. In the radio, we considered all measurements within the IXPE windows as well as those that took place less than half a day before the start or after the end of the IXPE observing times (i.e., all radio observations within MJD 59702.96 to MJD 59706.04, MJD 59733.99 to MJD 59736.94 and MJD 59736.90 to MJD 59739.88;

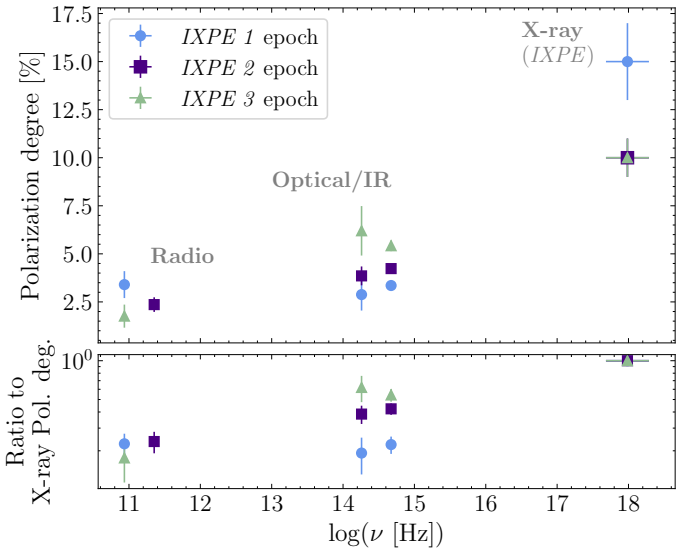

Fig. 3. Frequency dependency of the polarization degree. Top: MWL polarization degree as a function of frequency during all three IXPE epochs. Bottom: ratio of the frequency-dependent polarization degree to the corresponding X-ray polarization degree.

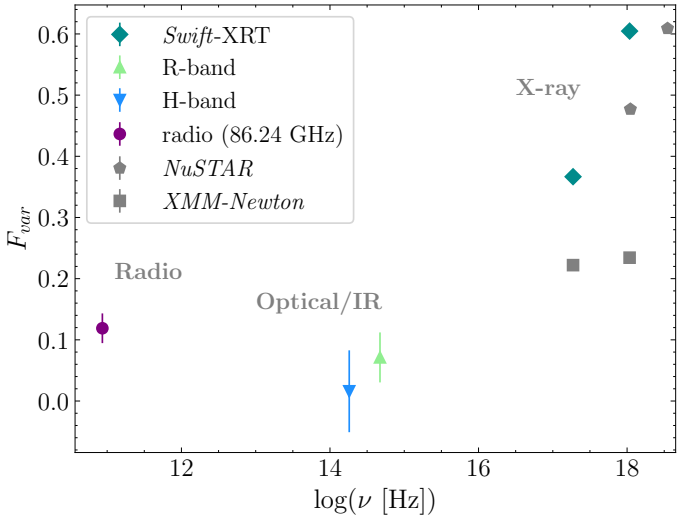

Fig. 4. Fractional variability ($F_{\rm var}$) as a function of the frequency during the IXPE epochs. $F_{\rm var}$ is computed using all data from Fig. 1 that are within the IXPE time windows. In the radio, we consider slightly relaxed simultaneity criteria and also include measurements that took place less than half a day before the start or after the end of the IXPE observing times (see the main text for more details). Radio, optical, IR, and *Swift* data are daily binned. We include the $F_{\rm var}$ from the *NuSTAR* and *XMM-Newton* multi-hour exposures using ≈30 min binning. These measurements are plotted in the gray since the two instruments did not gather data for all IXPE epochs, which biases the comparison with other wavebands.

May 3–7, 2022, June 3–6, 2022, and June 6–9, 2022). This more relaxed simultaneity criteria allows one to include radio measurements for IXPE 2 and IXPE 3 epochs, which do not contain strictly simultaneous radio polarimetry coverage. We note that the variability of the radio polarization throughout this campaign is anyhow low and happens on timescales longer than 1 day. Figure 3 highlights the energy dependence of the polarization degree, with an evident increase in the X-ray band, as already reported by Di Gesu et al. (2022) and Liodakis et al. (2022), both in Mrk 421 and Mrk 501.

All epochs share the common characteristics of a significantly higher polarization in X-rays compared to lower frequencies. This highlights the value of combining X-ray, optical and radio polarization data. We do not find any significant correlation of the polarization degree with the flux or spectral hardness in the individual energy bands. On the other hand, the ratio between the optical and IR polarization degree and the one in the X-ray band is significantly lower during IXPE 1 than during IXPE 2 and IXPE 3 (bottom panel of Fig. 3).

It is interesting to compare the broadband behavior of the polarization degree with the one of the fractional variability ($F_{\rm var}$; Vaughan et al. 2003). We computed $F_{\rm var}$ using all observations inside the IXPE windows, using the prescription of Poutanen et al. (2008) to estimate the corresponding uncertainties. The results are presented in Fig. 4. As for Fig. 3, we considered in the radio a slightly relaxed simultaneity criteria and also included measurements that took place less than half a day before the start or after the end of the IXPE observing times to compute $F_{\rm var}$. The $F_{\rm var}$ in the radio can only be computed with data from IRAM in the 86.24 GHz band since it is the only one that has more than one measurement (that is the minimum requirement for a computation of $F_{\rm var}$). In X-rays, we used *Swift*-XRT fluxes binned observation-wise in the 0.3–2 keV and 2–10 keV ranges. We complemented them with those from the *XMM-Newton* (0.3–2 keV and 2–10 keV) and *NuSTAR* (3–7 keV and 7–30 keV) long exposures. In these two cases, the results are plotted in gray markers to differentiate between them. Indeed, neither of the two instruments have simultaneous data for all IXPE epochs (unlike *Swift*-XRT), and given the generally stronger variability at those energies, this different temporal coverage biases the results and explains the discrepancy relative to the *Swift*-XRT $F_{\rm var}$.

Similarly to the polarization degree, $F_{\rm var}$ shows a significant increase in X-rays, while the optical and radio band are compatible within 1σ. This trend, previously reported in Mrk 421 and other HSPs (Aleksić et al. 2015a; Patel et al. 2018), potentially suggests an underlying physical origin common to the one explaining the broadband behavior of the polarization degree. A discussion on this aspect is given in Sect. 5.

3.5. Intra-night MAGIC and NuSTAR light curves during IXPE 2

During the night of June 5-6, 2022 (MJD 59734 to MJD 59735), MAGIC observations took place strictly simultaneously with *NuSTAR*. The light curves obtained are shown in Fig. 5. The data were divided into bins of around 30 min. Due to the otherwise limited exposure time by *NuSTAR*, the first bin was extended to ≈40 min. The upper panel shows the MAGIC fluxes, with an energy threshold of 400 GeV. This minimum energy is slightly higher than in Fig. 1 since some of the time bins contain observations taken under a zenith distance of up to 60°, which increases the energy threshold of the MAGIC stereo system. The *NuSTAR* fluxes were extracted in the 3–7 keV and 7–30 keV bands.

No significant intra-night variability can be claimed for the MAGIC observations. On the other hand, *NuSTAR* detects significant variability in both energy bands. By fitting the data with a constant model, the hypothesis of a non-variable emission is rejected at a significance above 5σ for the 3–7 keV band and above 3σ for the 7–30 keV band.

The flux measured by MAGIC is plotted against the flux of both *NuSTAR* energy bands in Fig. 6. The correlation coefficient

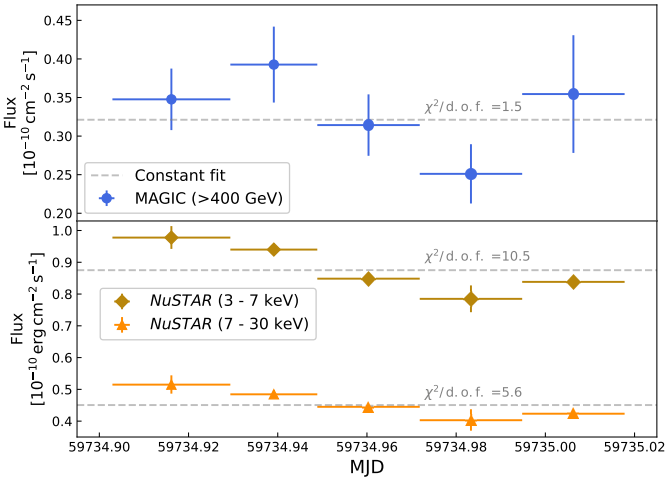

Fig. 5. MAGIC and *NuSTAR* intra-night light curve between June 4, 2022 (MJD 59734) and June 5, 2022 (MJD 59735), corresponding to the IXPE 2 epoch. Upper panel: Light curve above 400 GeV obtained with MAGIC. A constant model fit is showed in dashed gray with the corresponding reduced χ^2. Lower panel: Light curves for the 3–7 keV and the 7–30 keV band taken by *NuSTAR*, and constant fits for both. Fluxes from both instruments are computed in ≈30 min time bins, except for the first bin that is ≈40 min long due to a limited exposure of *NuSTAR* around at the start of the MAGIC observation.

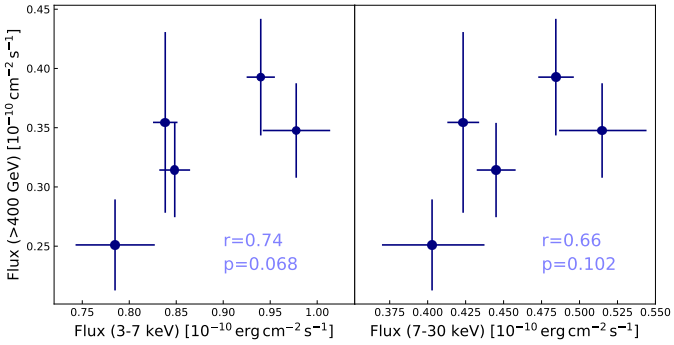

Fig. 6. MAGIC flux versus *NuSTAR* flux and quantification of the correlation during the IXPE 2 epoch. The MAGIC flux is computed above 400 GeV while the X-ray flux is evaluated in two different energy bands: 3–7 keV for the left panel and 7–30 keV for the right panel. In each panel, the obtained Pearson's r coefficient is indicated. We specify below the p-value that describes the probability of obtaining the observed r coefficient for two uncorrelated light curves. This p-value was estimated based on Monte Carlo toy simulations (see the main text for more details).

between each pair of energy bands is given by the Pearson's r coefficient. For the correlation between the 3–7 keV and >400 GeV flux a coefficient of $r = 0.74$, and between 7–30 keV and >400 GeV of $r = 0.66$ is found. Both cases suggest a light positive correlation. In order to evaluate the significance of the correlation, we used Monte Carlo simulated light curves. Each simulated flux point was produced by assuming a Gaussian distribution by taking the flux values of the actual data as a mean of the distribution and the uncertainty on the flux as the corresponding standard deviation. New light curves were then drawn and additionally the temporal information was shuffled in order to obtain pairs of "realistic" uncorrelated light curves. We simulated 10^6 pairs of light curves and derived p-values of the correlation coefficient r of the data based on the distribution of the r coefficients given by the simulations. We find a p-value of 0.068 (equivalent to $\approx 1.8\sigma$) between the 3–7 keV and >400 GeV bands and a p-value of 0.102 (equivalent to $\approx 1.6\sigma$) for 7–30 keV and >400 GeV. Due to the relatively large statistical uncertainties in the VHE light curve, no significant correlation can be claimed and only an indication of correlation at best can be proposed.

In Sect. 4 we extend the search for correlation over longer timescale by including data from the entire MWL campaign between April 2022 and June 2022.

3.6. Evidence of X-ray spectral hysteresis simultaneous to a polarization angle swing during IXPE 2 and IXPE 3

Using the multi-hour exposure of *NuSTAR*, we investigate in detail the X-ray spectral evolution during the period where a polarization angle swing is detected by IXPE in the X-rays (see Sect. 3.2 and Fig. 1). Figure 7 is a zoomed-in view of around the polarization angle swing, showing the *NuSTAR* measurements together with the polarization degree and angle in the radio, optical and IR. For IXPE, the polarization degree and angle were binned in ∼3 h.

The top panel shows the *NuSTAR* fluxes in the 3–7 keV and 7–30 keV bands, in 1 h time bins. Small variability is noted during the observation from June 5 to 6, 2022 (MJD 59734 to MJD 59735, simultaneous to IXPE 2), but more structured variability patterns can be seen during the observation simultaneous to IXPE 3, between June 8 and 9, 2022 (MJD 59737 to MJD 59738). In particular, the light curve displays two "humps" caused by two consecutive flux rise and decay phases, which thus reveal variability on ∼1 h timescale.

The *NuSTAR* spectra were fitted in the 3–30 keV band adopting a log-parabola model (pivot energy fixed at 1 keV). By fitting the spectra with a 1 h temporal binning, we find that the curvature parameter β shows little variability throughout the observations. The derived β values range from 0.27 to 0.57, but for each time bin they are within less than $\approx 2\sigma$ from the weighted average over the two observations, which yields $\beta_{\rm avg} = 0.45$. Consequently, we performed a second series of fits with a 1 h binning after fixing $\beta = 0.45$ to remove any correlation between α and β in order to obtain a more straightforward assessment of the spectral hardness evolution. We stress that fixing $\beta = 0.45$ does not significantly degrades the fit statistics (the beta-free spectral model is preferred at a significance below 2.5σ in each of the bins). The resulting index α as a function of time in 1 h bins is plotted in the second panel from the top in Fig. 7.

For the observation simultaneous to the IXPE 2 period (around MJD 59735 – June 5, 2022), we do not find strong spectral change. The index α varies by at most 5% around a value of ≈ -2.35, during a quasi-monotonic flux decay of ≈30%. We do not detect any significant correlation between α and flux, nor any spectral hysteresis pattern.

Regarding the *NuSTAR* observations taken at the same time as the IXPE 3 period, a similar spectral variability amplitude is observed, although hysteresis patterns can be seen when α is reported as a function of the flux. Figure 8 shows the value of α versus the 3–7 keV and 7–30 keV fluxes in 1 h bins during IXPE 3. The gray arrows indicate the direction of time. During the first part of the observation, the data points (both in the 3–7 keV and 7–30 keV bands) display a spectral hysteresis in a clockwise direction (i.e., decay phase has softer spectrum than in the rising phase). On the other hand, the second part of the observations exhibits a spectral hysteresis in counterclockwise direction (i.e., decay phase has a harder spectrum than in the rising phase). Spectral hysteresis, in both the clockwise and counterclockwise direction, has been previously detected in

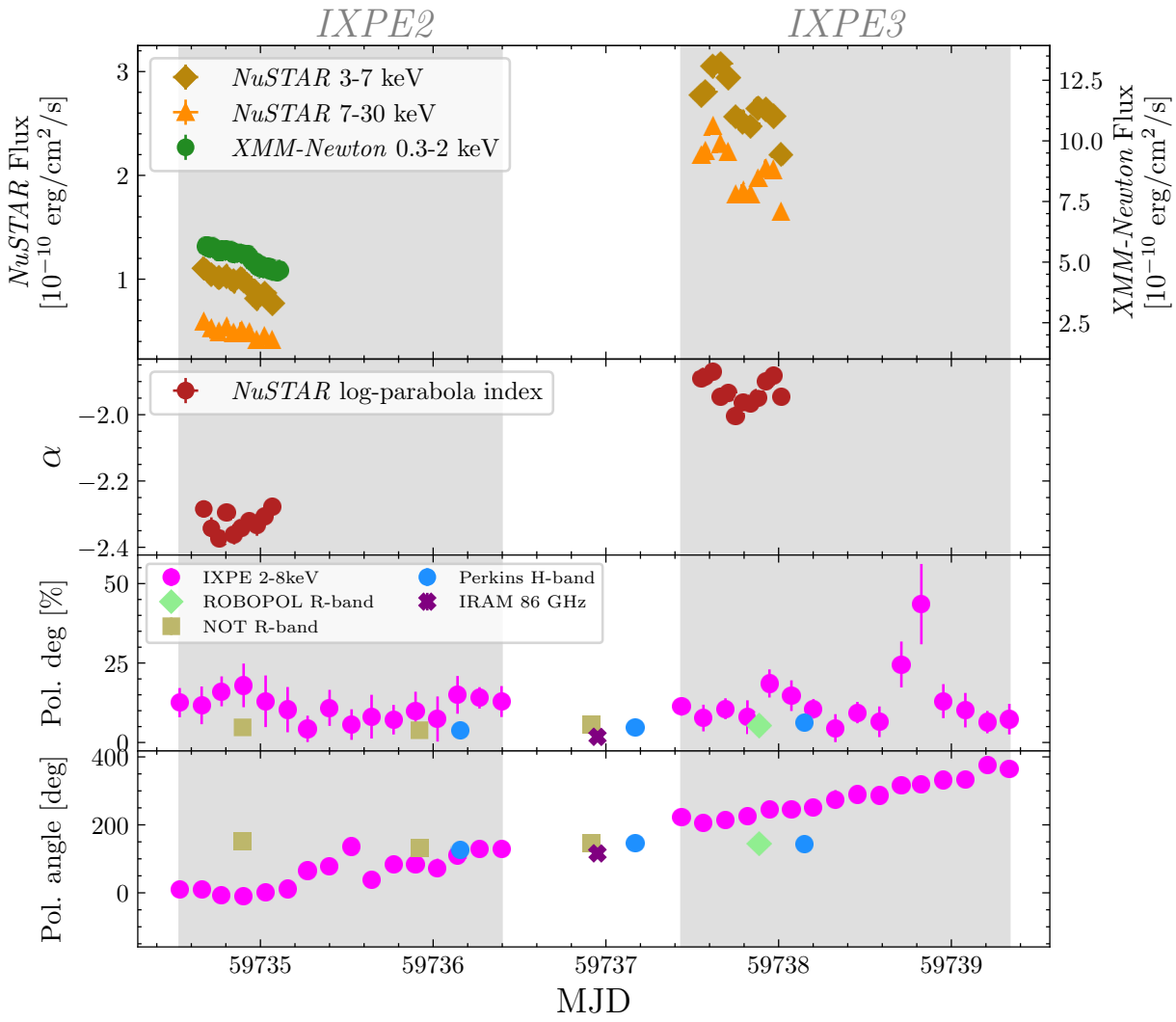

Fig. 7. Zoomed-in view of the *NuSTAR* light curves in the 3–7 keV and 7–30 keV bands during the IXPE 2 and IXPE 3 epochs. The top panel report the fluxes in 1 h bins. The second panel from the top is the α index evolution derived from fits of the *NuSTAR* spectra. The last two panels show the simultaneous polarization degree and polarization angle in the X-ray band (IXPE), optical and radio bands.

Mrk 421 (Brinkmann et al. 2003; Ravasio et al. 2004). Nonetheless, it is the first time that two continuous clockwise and counterclockwise rotations are detected over an hour timescale. A more detailed discussion of these results is given in Sect. 5.

As unveiled by the bottom panels of Fig. 7, no significant variability is observed in the polarization degree simultaneous to the *NuSTAR* hysteresis patterns. Based on a constant fit, the data are consistent with a stable X-ray polarization hypothesis within 3σ (both for IXPE 2 and IXPE 3 periods). Regarding the X-ray polarization angle, the large angular swing mentioned before happens at a constant speed of ∼80°/day despite the *NuSTAR* flux and variability patterns discussed above.

4. MWL evolution and correlation throughout the observing campaign

As commonly seen in HSPs such as Mrk 421, the flux (Fig. 1) displays the strongest variability in the X-ray and VHE regimes. A noticeable feature in the MAGIC light curves is an enhanced VHE state period between MJD 59719 (May 20, 2022) and MJD 59723 (May 24, 2022). A peak flux of ∼1.4 C.U. is measured on MJD 59722 (May 23, 2022) in both the 0.2–1 TeV and >1 TeV bands (equivalent to ≈3 times the typical state). A simultaneous significant flux increase is noted in X-rays, as revealed by the *Swift*-XRT light curves (third panel from the top). This high state also coincides with a hardening of both the VHE and X-ray spectrum, as illustrated by the hardness ratio plotted in the fourth panel from the top. This behavior, already seen within the IXPE observing epochs in the earlier section, is consistent with the harder-when-brighter trend previously detected in Mrk 421 (Aleksić et al. 2015a; Acciari et al. 2021; MAGIC Collaboration 2021). At lower energies, no simultaneous outburst is detected in the UV and optical (seventh and eighth panel from the top). On the other hand, it is interesting to remark that a RoboPol measurement (*R*-band) simultaneous to the peak activity at VHE on MJD 59722 (May 23, 2022) shows a rotation of the polarization angle by about 60° compared to an observation conducted a few days earlier (∼MJD 59718 – May 19, 2022). Such a swing of the polarization angle of comparable amplitude and on similar timescales (i.e., an approximately daily timescale) was reported by Marscher & Jorstad (2021) in 2017, also for Mrk 421. The sparse sampling of the RoboPol light curve prevents, however, a strong claim on the association of the optical polarization angle rotation with the VHE and X-ray flare. Besides the enhanced

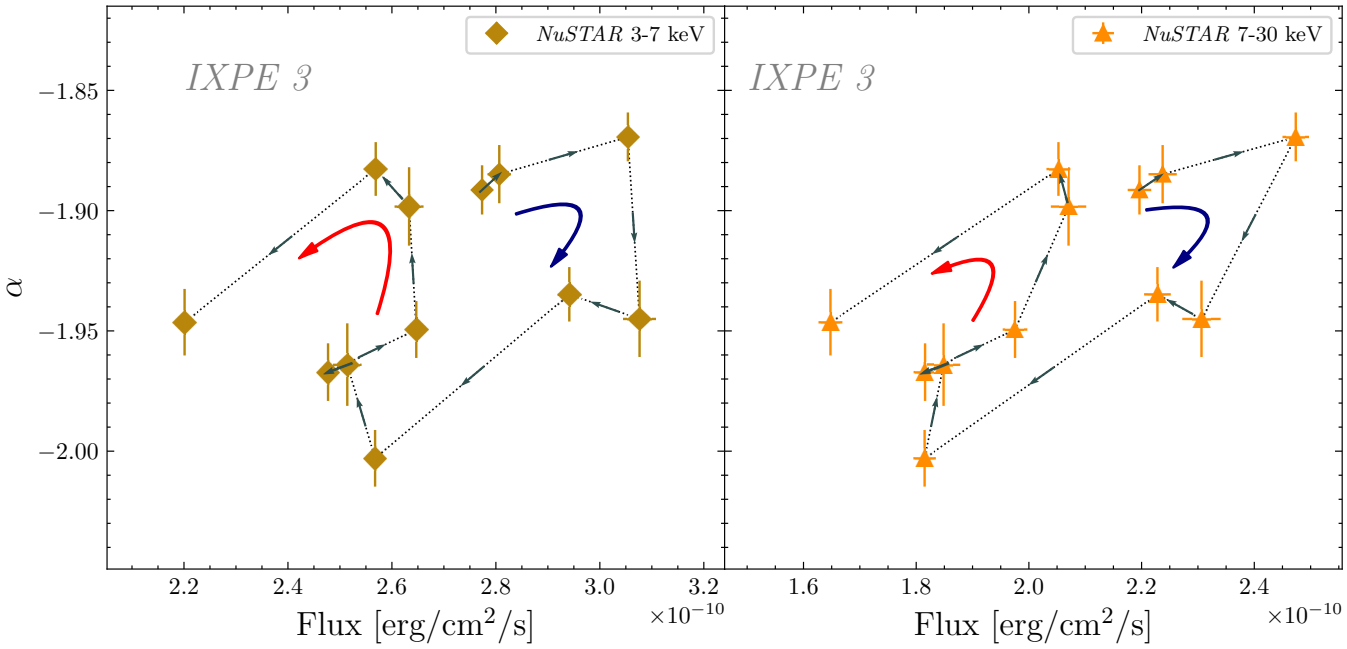

Fig. 8. Log-parabola photon index, α, versus 3–7 keV and 7–30 keV flux as measured by *NuSTAR* during the third IXPE observation (IXPE 3 period). The data are 1 h binned and α is obtained by fitting a log-parabola function that has a fixed curvature parameter $\beta = 0.45$. The gray arrows show the direction of time, and the blue and red arrows in the middle of the panels depict the clockwise and counterclockwise directions observed in the data, respectively.

state around MJD 59722 (May 23, 2022), the emission in the X-ray and VHE bands along the campaigns remains comparable to the quiescent activity. In fact, during previous outbursts, the VHE and X-ray fluxes were more than an order of magnitude higher than the average value from the campaign discussed in this work (Acciari et al. 2020; Abeysekara et al. 2020).

In the 0.3–300 GeV band, the *Fermi*-LAT light curve exhibits a flux variability by a factor of ∼3 around an average state of $\sim 8 \times 10^{-8}$ cm^{-2} s^{-1}, which is close to the typical flux level for Mrk 421 (Aleksić et al. 2015a). As for the spectral evolution, no significant variability of the *Fermi*-LAT power-law index is detected.

In the UV band, despite moderate variability, the *Swift*-UVOT fluxes display an interesting quasi-monotonic increase starting from MJD ∼59710 (May 11, 2022) to MJD ∼59760 (June 30, 2022). The highest UV state is registered on MJD 59753 (June 23, 2022), and slightly more than twice the minimum state is measured on MJD 59717 (May 18, 2022). The *R*-band measurements show a similar increasing trend over this period. Over the same period, the X-ray band shows an opposite evolution with an overall decay of the 0.3–2 keV and 2–10 keV fluxes. This behavior is accompanied by a simultaneous drop of the X-ray hardness ratio (see the fourth panel from the top in Fig. 1). Such a behavior points toward an anticorrelation between the X-ray and UV bands, possibly caused by a shift of the entire synchrotron component to lower frequencies. The quantification of the anticorrelation significance is performed in Sect. 4.2.

4.1. VHE–X-ray correlation over the entire campaign

In Sect. 3.5 we reported an indication of positive correlation between the MAGIC and *NuSTAR* fluxes during the IXPE 2 observations. The low significance (estimated around 2σ between the 3–7 keV and >400 GeV bands) is partly due to the relatively large uncertainties on the VHE gamma-ray fluxes measured in these short timescales. In this section, we extend the VHE versus X-ray correlation study over the entire campaign by making use of the MAGIC and *Swift*-XRT measurements. We correlated the daily binned MAGIC fluxes (in the 0.2–1 TeV and >1 TeV bands) with the *Swift*-XRT fluxes binned observation-wise (0.3–2 keV and 2–10 keV bands), and computed the discrete correlation coefficient (DCF; Edelson & Krolik 1988) in a series of 2-day binned time lags. The significance of the DCF was estimated based on Monte Carlo simulations. The simulations were performed in a similar fashioned to what is described in MAGIC Collaboration (2021). We summarize below the procedure.

The significance bands were obtained by first simulating a large number (10^4) of uncorrelated light curves for each of the energy bands considered. The light curves were simulated using the prescription from Emmanoulopoulos et al. (2013) in order to preserve the probability distribution function of the observed fluxes. Furthermore, the simulated light curves were produced by assuming a power spectral density (PSD) function that follows a power-law model. The slopes of the PSD models in X-rays were taken directly from MAGIC Collaboration (2021) and are −1.45 for the 0.3–2 keV band and −1.3 for the 2–10 keV band. These slopes (derived with *Swift*-XRT data in 2016-2017 that cover a longer time span than the one considered in this work) were found to be in agreement with the 2022 observations and thus represent a good proxy to estimate the significance. Regarding the simulations of VHE light curves, it was not possible to directly extract the PSD slope in a reliable manner using the MAGIC data of this work due to the relatively sparse sampling. We therefore adopted the PSD slope of −1.3 that was reported by (Aleksić et al. 2015a) using Whipple observations during a campaign organized in 2009. The fake light curves were

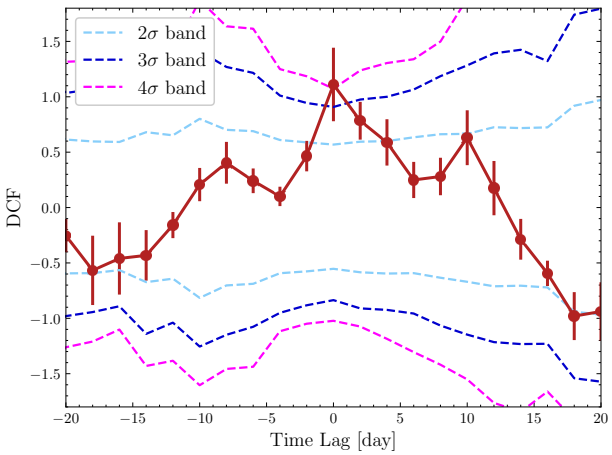

Fig. 9. DCF computed for the MAGIC 0.2–1 TeV and *Swift*-XRT 2–10 keV light curves between MJD 59700 (May 1, 2022) and MJD 59740 (June 10, 2022) with a time-lag binning of 2 days. The red points are the obtained DCF values and their uncertainties. The light blue, dark blue, and pink dashed lines show the 2σ, 3σ and 4σ significance bands, respectively (see the main text for more details).

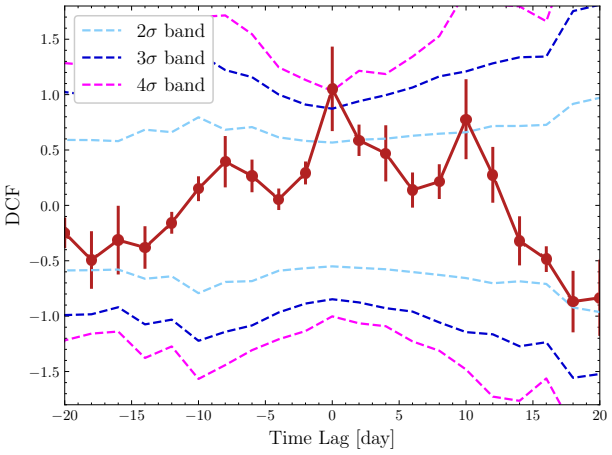

Fig. 10. DCF computed for the MAGIC >1 TeV and *Swift*-XRT 2–10 keV light curves between MJD 59700 (May 1, 2022) and MJD 59740 (June 10, 2022) with a time-lag binning of 2 days. The red points are the obtained DCF values and their uncertainties. The light blue, dark blue, and pink dashed lines show the 2σ, 3σ and 4σ significance bands, respectively (see the main text for more details).

generated with a temporal resolution matching the typical exposure time of the observations, and the same temporal sampling as the data was then applied to the simulations. Finally, we computed the DCF as a function of time lag for all pairs of simulated light curves. The 2σ, 3σ, and 4σ confidence bands were derived from the distribution of the simulated DCF values in each time-lag bin.

Figures 9 and 10 show the DCF obtained from MAGIC 0.2–1 TeV versus *Swift*-XRT 2–10 keV and MAGIC >1 TeV versus *Swift*-XRT 2–10 keV, respectively. The dashed lines depict the 2σ (light blue), 3σ (dark blue), 4σ (magenta) confidence bands. A positive correlation can be seen at zero time lag with a significance of 4σ, further strengthening the reported in Sect. 3.5. As for the correlation of the MAGIC fluxes with the 0.3–2 keV band, the significance is somewhat lower, around 3σ. The results are shown in Figs. B.1 and B.2. This suggests that the 2–10 keV flux is more closely related to the VHE flux compared to the 0.3–2 keV band during this period of time.

4.2. Investigation of the UV and optical versus X-ray anticorrelation

Figure 1 suggests an anticorrelation between the UV and X-ray fluxes between MJD 59710 (May 11, 2022) and MJD 59760 (June 30, 2022). We quantify this trend by computing the DCF between the *Swift*-XRT data (using both the 0.3–2 keV and 2–10 keV fluxes) and the *Swift*-UVOT $W1$ measurements. For simplicity, only the data in the *Swift*-UVOT $W1$ band were considered for this correlation study. In fact, the fluxes in the $M2$ and $W2$ *Swift*-UVOT filters give very similar results, which is expected given their proximity in frequency with $W1$. The resulting plots are shown in Figs. C.1 and C.2 for the 0.3–2 keV and 2–10 keV bands, respectively. The significance bands were obtained with the exact same method described in the previous section. The PSD slopes were taken from MAGIC Collaboration (2021): −1.45 for *Swift*-UVOT $W1$ and *Swift*-XRT 0.3–2 keV and −1.3 for *Swift*-XRT 2–10 keV. We find that the significance of the anticorrelation observed in the data is at the level of $2–3\sigma$, and can only be considered marginal evidence. The significance is marginally higher in the *Swift*-UVOT $W1$ versus *Swift*-XRT 2–10 keV case than in the *Swift*-UVOT $W1$ versus *Swift*-XRT 0.3–2 keV case. The peak at a positive time lag of ∼16 days in both figures, can be considered an artifact resulting from the sampling and short overall time period.

We repeated the above exercise after including *Swift* data from the entire MWL campaign (i.e., from MJD 59695 to MJD 59760; April 26, 2022, to June 30, 2022). The results – shown in Figs. C.3 and C.4 – reveal a decrease in the significance below 2σ. The marginal evidence of anticorrelation is thus only observed over a 1.5-month period between MJD ∼59710 (May 1, 2022) and MJD ∼59760 (June 30, 2022).

This is the third time that an indication of anticorrelation between UV and X-ray fluxes is reported in Mrk 421. The first two hints were observed during MWL campaigns organized during 2009 (Aleksić et al. 2015a) and 2017 (MAGIC Collaboration 2021), and were also happening over an approximately monthly timescale. These repeating trends point toward some physical connection between the UV and X-ray emitting regions, which is particularly relevant in the context of the recent IXPE results that suggest energy-stratified emitting regions.

The anticorrelation is not significantly detected during the first part of the 2022 campaign, which might be explained by a low variability. Alternatively, the physical mechanism responsible for the anticorrelation may only take place temporarily. MAGIC Collaboration (2021) investigated the anticorrelation between X-ray and UV as well as X-ray and optical over several months. They also found that such a trend became significant on ∼monthly timescales, possibly indicating that it is not a permanent feature of Mrk 421.

4.3. Optical polarization evolution throughout the entire campaign

The R-band flux, which is close to the UV in frequency, also displays an increase throughout the campaign, in particular during the second part (between MJD 59710 and MJD 59760; May 11, 2022, to June 30, 2022), corroborating the anticorrelation hinted at by the *Swift*-UVW1 measurements. The R-band data are unfortunately too sparse to properly quantify the trend in that waveband. The rise in the optical flux seems to

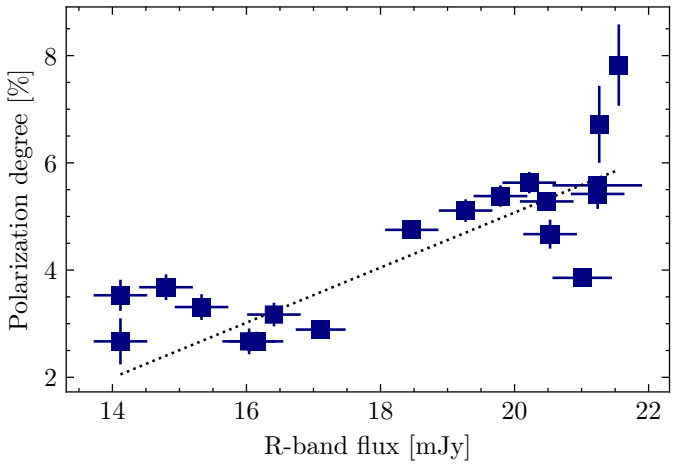

Fig. 11. Correlation between the polarization degree and flux in the R band over the entire campaign. The dotted black line is a linear fit, yielding a best-fit slope of $a = 0.52 \pm 0.09$. The Pearson's r of the correlation is $r = 0.8 \pm 0.1$. The associated p-value is $p_{\rm value} = 1 \times 10^{-5}$.

be accompanied by an increase in the polarization degree. In Fig. 11, we present the correlation between the polarization degree and flux using strictly simultaneous R-band measurements. We considered all data from RoboPol, NOT and T90 along the campaign. The KANATA measurements were discarded because of their very large flux uncertainties, in comparison to the measurements from the other instruments. We stress that the data mostly cover the MJD 59710 to MJD 59760 period (i.e., during the UV and X-ray anticorrelation hint period; May 11, 2022, to June 30, 2022), except for a single NOT measurement that took place before (on MJD 59703 – May 4, 2022). We find a positive correlation with a Pearson's r of $r = 0.8 \pm 0.1$. Using the same method as in Sect. 3.5, we estimated an associated p-value of $p_{\rm value} = 1 \times 10^{-5}$, corresponding to a correlation significance of $\approx 4\sigma$. By fitting a linear function (see the dotted black line), the slope of the correlation is $a = 0.51 \pm 0.09$. The same results are derived if one considers data between MJD 59710 to MJD 59760 (i.e., after removing the NOT measurement on MJD 59703).

Overall, the combination of the UV versus X-ray anticorrelation on approximately monthly timescales and the rise in the R-band polarization degree observed over similar timescales potentially implies a general change in the physical properties of the source. The interpretation of this observation is given in Sect. 5.

5. Discussion and summary

This work reports on an extensive MWL observation campaign of Mrk 421 organized in 2022 from the radio to VHE gamma rays, including, for the first time, a simultaneous characterization of the X-ray polarization behavior. The VHE observations were carried out using the MAGIC telescopes and are accompanied by observations from *Fermi*-LAT, *NuSTAR*, *XMM-Newton*, and *Swift* as well as multiple instruments covering the optical to radio bands.

The daily coverage from MAGIC during the first IXPE observation in May 2022 (IXPE 1) reveals a low emission state at VHEs ($\approx$25% of the Crab Nebula in the 0.2–1 TeV band) without any significant variability on either day or hour timescales. Moderate daily variability is noted in the X-ray band, which reveals an emission state lower than the average activity of Mrk 421 (Abdo et al. 2011). The optical, UV and MeV-GeV fluxes remain close to the typical activity. As for the broadband polarization characteristics, the polarization degree is significantly stronger in X-rays than at lower frequencies. This illustrates the importance of combining X-ray, optical and radio polarization data. As discussed in Di Gesu et al. (2022) and Liodakis et al. (2022), these results are in line with an energy-stratified jet, where the most energetic particles (emitting X-ray photons) are located in smaller regions that possess a more ordered magnetic field, close to the acceleration site. The energy dependence and the slow variability of the polarization degree strongly point toward a shock acceleration scenario. Electrons subsequently cool and diffuse in larger regions, where the field is more turbulent, and continue to emit from optical to radio frequencies. During IXPE 1, there is no significant variation in the polarization angle (Di Gesu et al. 2022) at any energy. In particular, the X-ray polarization angle is compatible with that measured in the optical and radio.

The IXPE 2 and 3 epochs (June 2022) are also characterized by a constant X-ray polarization degree that is significantly higher compared to lower frequencies. Such a general broadband feature of the polarization degree shares some similarities with the variability strength (quantified with the fractional variability, $F_{\rm var}$), which also shows an increase with energy. The $F_{\rm var}$ during the IXPE exposures is indeed significantly higher in the X-ray band compared to the optical and radio data. This behavior may partially be caused by an X-ray emission dominated by (a single or a few) compact regions whose temporary appearance within the jet drives the observed variability, while emission at lower frequencies receives simultaneous contributions from several broader regions that decrease the overall variability. Such a scenario corroborates the energy stratification of the jet implied by the energy dependence of the polarization strength.

While the IXPE 2 and 3 epochs are consistent with a constant polarization degree, the polarization angle exhibits an evident rotation in X-rays during these two IXPE exposures. The rotation proceeds at a constant angular velocity (see also Di Gesu 2023) between the two epochs, and hence is highly suggestive of a single rotation event observed during the two consecutive IXPE 2 and 3 exposures. The optical and radio observations do not show a simultaneous angle rotation.

We managed to characterize the VHE state only at the very beginning of the polarization angle rotation. During that time period, we find that the VHE emission state is higher (and the spectrum is harder) than during IXPE 1, albeit comparable to the average for the source ($\approx$50% of the Crab Nebula in the 0.2–1 TeV band; Abdo et al. 2011). Starting from the second half of the IXPE 2 epoch and during IXPE 3, the activity in X-rays increases and hardens significantly, simultaneously with the angle rotation. The emission reaches a maximum well above the Mrk 421 quiescent state. The VHE gamma rays usually show a strong correlation with X-rays, especially during X-ray flaring activities, as observed during IXPE 3 (see, e.g., Acciari et al. 2020), but the lack of simultaneous observations with MAGIC prevents us from evaluating this characteristic during this specific flaring activity in June 2022.

Previous campaigns on LSP and ISP objects have shown that rotations of the polarization angle in the optical can be associated with flares (Ahnen et al. 2017a; MAGIC Collaboration 2018; Abdo et al. 2010b; Gupta et al. 2019; Chandra et al. 2015; Marscher et al. 2008). In LSPs and ISPs, the synchrotron peak is located around the optical band, while in HSPs (as Mrk 421) it is located in the X-ray regime. One would thus naively expect that X-ray flares in HSPs can similarly be associated with X-ray

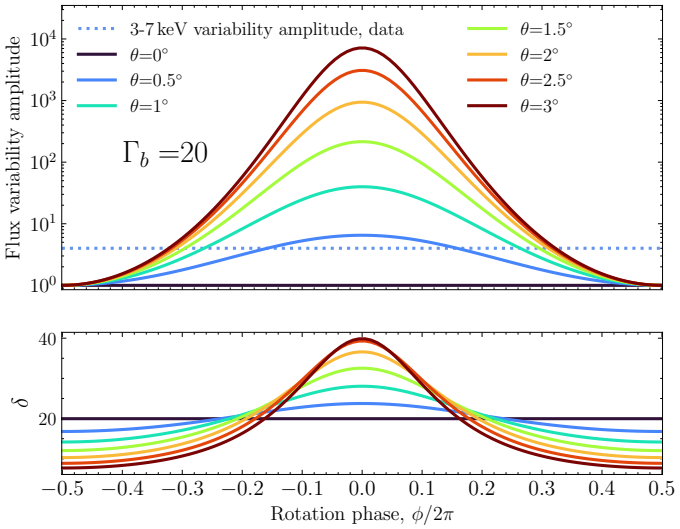

Fig. 12. Relativistic beaming effects due to the travel along a helical path within the jet. Top panel: Flux variability amplitude caused by the evolution of the Doppler factor, δ, when an emitting zone is traveling downstream along a helical path. The variability amplitude is plotted as a function of the phase of the spiral rotation. The horizontal dotted blue line gives the observed variability amplitude in the 3–7 keV band. Bottom panel: Corresponding Doppler factor, δ, as a function of the spiral rotation phase. The curves are produced for different jet axis angles (θ) relative to the line of sight. The zone is assumed to move with a Lorentz factor $\Gamma_b = 20$ in a helical field with a pitch angle of 2.9° (see the main text for more details).

polarization angle swings. Even if the enhanced X-ray state during IXPE 2 and 3 remains below that of previous notable outbursts of Mrk 421 (see for instance the March 2010 flare reported in Aleksić et al. 2015b), the evident X-ray flux rise and hardening, temporally coincident with a polarization angle swing, may share a common physical origin with the angular swings observed in lower synchrotron peaked blazars.

The absence of a simultaneous polarization angle swing in the optical, IR and radio may be explained by the following scenario: the smaller region radiating the X-ray photons (where the B field is more ordered) is streaming down the jet following helical field lines, leading to an apparent rotation of the polarization angle (Di Gesu 2023), while at lower frequencies, the emitting regions are larger and do not closely follow a helical path, unlike the X-ray region.

The movement of a compact region through a helical path inside the jet induces changes in the Doppler factor, which then lead to significant observed flux variability. We thus investigated whether such a scenario, proposed to explain the angle rotation, is (roughly) consistent with the observed variability amplitude in the X-rays (that is, the energy range with the best temporal coverage during the rotation). The viewing angle, ψ, of a region streaming down a helical path is given by (see, e.g., Larionov et al. 2013)

$$\psi = \arccos\left[\cos\theta\cos\zeta + \sin\theta\sin\zeta\cos\phi\right], \quad (2)$$

where θ is the jet axis angle to the line of sight, ζ the pitch angle of the helical field, and ϕ the phase of the spiral rotation. If the region moves at a Lorentz factor of Γ_b, the associated Doppler factor is $\delta = [\Gamma_b(1-\beta\cos\psi]^{-1}$. In the observer's frame, the intrinsic flux, $F_{\rm intr}$, transforms as (Rybicki & Lightman 1979)

$$F_{\rm obs} = \delta^{3+p} F_{\rm intr}, \quad (3)$$

where p is the photon index, which we found to be around −2.4 in the 3–7 keV band of *NuSTAR* during the rotation. According to Di Gesu (2023), the rotation rate can be reproduced if the emitting feature travels with a velocity component parallel to the jet axis of $0.9975c$ and a transverse component of $0.05c$. Based on this estimation, the corresponding pitch angle of the helical field is ≈2.9°. Assuming a typical Lorentz factor of $\Gamma_b = 20$, the expected flux variability amplitude solely introduced by an evolution of the Doppler factor due to the movement on a helical path is plotted in the top panel of Fig. 12. The variability is plotted as a function of the phase of the rotation. The curves are plotted for a set of θ ranging from 0° to 3°, which is typical for blazars. The variability amplitude, being a few orders of magnitude higher for $\theta = 3°$, is strongly dependent on the jet viewing axis. The horizontal dotted blue line displays the observed flux amplitude in the 3–7 keV band, which can be explained by the change in Doppler factor if $\theta \approx 0.5°$. The low apparent speed of radio knots in Mrk 421 suggests that very long baseline radio observations mostly probe the sheath of the jet instead of the central part (i.e., the spine; see, e.g., Ghisellini et al. 2005; Weaver et al. 2022). We note, however, that Weaver et al. (2022) estimated $\theta \sim 1°$, which is relatively consistent with Fig. 12. One concludes that, assuming relatively standard parameters, the observed flux changes are not in contradiction with the variability caused by the evolution of the Doppler factor (as the zone travels on helical field lines). It is important to note that the flux variability is also likely affected by acceleration and cooling processes, as suggested by the spectral changes observed on approximately day to hour timescales in the *NuSTAR* data during IXPE 2 and 3. Hence, the MWL data tell us that the changes in the δ cannot be the only reason for the observed flux variability.

The observations by *NuSTAR* simultaneous to the polarization angle swing during IXPE 3 reveal two contiguous spectral hysteresis loops in opposite directions over a single exposure (see Fig. 8). The first loop, in a clockwise direction, is likely the signature of synchrotron cooling causing a delay of the low-energy X-ray photons with respect to the high-energy ones (soft lag). The subsequent counterclockwise loop indicates a delay of the high-energy X-ray photons compared to the low-energy ones (hard lag), suggesting a system observed at energies for which the acceleration timescale is comparable to the cooling timescale, $t'_{\rm acc} \approx t'_{\rm cool,synch}$ (Kirk et al. 1998).

Within a framework of shock acceleration, as suggested by the multiband polarization properties, the acceleration timescale in the co-moving frame (primed quantities) of an electron with Lorentz factor γ can be approximated as follows (Drury 1983; Blandford & Eichler 1987; Kusunose et al. 2000):

$$t'_{\rm acc} = \frac{20\lambda(\gamma)c}{3u_{\rm s}^2}, \quad (4)$$

where $\lambda(\gamma) = \frac{\xi\gamma m_{\rm e}c^2}{eB'}$ is the mean free path of electrons, parameterized as a fraction, ξ, of the Larmor radius. The parameter ξ, sometimes dubbed the gyro-factor, is related to the efficiency in the acceleration of the high-energy particle population and is always ≥1. In the so-called Bohm limit, the acceleration is the most efficient because it occurs over a mean free path similar to the Larmor radius, and $\xi = 1$. Within this framework, the acceleration efficiency is proportional to ξ^{-1}, and $\xi > 1$ indicates an acceleration efficiency lower than that in the Bohm limit. B' is the magnetic field inside the emitting region and $u_{\rm s}$ the speed of the shock, which we assume to be relativistic, $u_{\rm s} \sim c$. The

synchrotron cooling time is given by

$$t'_{\rm cool,synch} = \frac{3m_e c}{4\sigma_T U'_B \gamma} = \frac{6\pi m_e c}{\sigma_T B'^2 \gamma}, \quad (5)$$

where σ_T is the Thomson cross section and $U'_B = B'^2/8\pi$ the magnetic field energy density. By expressing the timescales in terms of the observed photon energy, and considering that electrons emit most of their synchrotron photons at an observed frequency of $\nu \approx 3.7 \times 10^6 \frac{\gamma^2 B' \delta}{1+z}$, where δ is the Doppler factor of the emitting region, one finds that the ratio $t_{\rm acc}/t_{\rm cool,synch}$ is in fact independent of B' (Zhang et al. 2002):

$$\frac{t_{\rm acc}}{t_{\rm cool,synch}}(E) = 3.17 \times 10^{-5}(1+z)\xi\delta^{-1}E \quad {\rm s}, \quad (6)$$

where E is the photon energy in keV units. The counterclockwise loop observed by *NuSTAR* implies $t_{\rm acc}/t_{\rm cool,synch} \approx 1$ at $E \approx 10$ keV, which is the characteristic energy probed by *NuSTAR*. Assuming a typical $\delta = 30$ for Mrk 421, one thus derives $\xi \approx 8\times10^4$ for the second part of the *NuSTAR* observation during the IXPE 3 epoch.

On the other hand, the first part of the *NuSTAR* observation in the IXPE 3 epoch, where a clockwise loop is observed, suggests a regime in which $t_{\rm acc}/t_{\rm cool,synch} \ll 1$ since synchrotron cooling is likely the driver of soft lags. The acceleration must take place in a significantly more effective manner. During this part of the observation, ξ must therefore be at least an order of magnitude smaller, $\xi \lesssim 8 \times 10^3$. While the range of values we derive for ξ stays within the estimates of Baring et al. (2017), where it is discussed in a broader theoretical context, the consecutive clockwise and counterclockwise loops during IXPE 3 imply an increase in the gyro-factor, ξ, of at least one order of magnitude over approximately hour timescales.

The above calculations and estimations of ξ do not consider IC cooling. We verified that such a simplification does not significantly affect our results. Using a SSC model (Maraschi et al. 1992; Madejski et al. 1999) that we constrained using the X-ray and VHE spectra during the IXPE epochs, we estimate that the IC cooling timescale is longer than the synchrotron cooling timescale, as one would in any case expect from the lower luminosity of the IC bump in comparison to that of the synchrotron bump. Our model in fact shows a synchrotron cooling timescale that is about twice shorter than the IC cooling. Hence, the synchrotron cooling is sufficient to estimate the dynamics of the electrons, and Eq. (6) remains a valid approximation for estimating ξ. A detailed description of the model and the computation is given in Appendix D.

The modeling performed in Appendix D constrains the magnetic field to be $B' \sim 0.04$ G in the X-ray and VHE emitting region with a blob radius of $R' \approx 2 \times 10^{16}$ cm. These values imply a synchrotron cooling time (Eq. (5)) longer than the light-crossing time ($t'_{\rm cr} = R'/c$) for electrons emitting up to ≈10 keV, which is well within the *NuSTAR* bandwidth. The modeling parameters are thus clearly in agreement with a *NuSTAR* variability regulated by cooling (and/or acceleration) mechanisms, instead of the light-crossing time effects, in line with what is suggested by the observed hysteresis loops. If the light travel time is significantly longer than the cooling and/or acceleration timescale, the variability will be dominated via the former.

As a final consideration, we combined Eq. (5) with the characteristic synchrotron frequency ($\nu \approx 3.7\times10^6 \frac{\gamma^2 B' \delta}{1+z}$) to derive the expected cooling timescale in the observer's frame (Zhang et al. 2002):

$$t_{\rm cool,synch}(E) = 3.04 \times 10^3 B'^{-3/2}(1+z)^{1/2}\delta^{-1/2}E^{-1/2} \quad {\rm s}. \quad (7)$$

The parameters from the modeling in Appendix D give $t_{\rm cool,synch}(E = 3\,{\rm keV}) \approx 11$ h and $t_{\rm cool,synch}(E = 10\,{\rm keV}) \approx 6$ h, which is again consistent with the flux doubling and/or halving timescale derived by the *NuSTAR* data.

Within the IXPE observing windows, there is an indication of stronger optical and IR polarization for IXPE 2 and IXPE 3 compared to IXPE 1. IXPE 2 and 3 also exhibit a ratio between the optical, IR and X-ray polarization degree that is significantly higher. In the configuration of an energy-stratified jet, this possibly indicates that the optical emission originates from regions that are closer to the shock, where the magnetic field is more ordered (i.e., closer to the X-ray emitting region), while for IXPE 1 the optical flux is emitted farther downstream in the jet.

By exploiting data from the entire MWL campaign, we find a positive correlation at the level of 4σ between X-rays and VHE gamma rays without any time delay between the MAGIC energy bands and the 2–10 keV band of *Swift*-XRT. The correlation is at the level of 3σ with the 0.3–2 keV band. The positive correlation without a time lag supports leptonic scenarios in which the same electron population produces the X-ray and VHE emission, via the SSC process. Positive correlations at zero time lags were also reported in several previous studies (MAGIC Collaboration 2021; Arbet-Engels et al. 2021; Acciari et al. 2021; Aleksić et al. 2015a). Such a positive correlation suggests that VHE gamma rays are also emitted close to the shock front (co-spatially to the X-rays). The higher significance obtained when using the X-ray 2–10 keV band instead of the 0.3–2 keV band suggests that the VHE emission has a tighter relation with the X-ray fluxes above a few keVs rather than below that. Looking at Fig. 2, this implies that the falling edge of the high-energy SED component is mostly dominated by electrons that emit synchrotron photons well above $\nu_{\rm p}$, which is in agreement with the expectation of leptonic scenarios (Tavecchio et al. 1998).

At lower energies, we find marginal evidence of an anticorrelation between the X-ray and UV fluxes from May 2022 to June 2022. In this time span, while the X-ray emission shows a long-term flux decay and spectral softening, the UV emission is rising with a quasi-monotonic trend. We find that the marginal evidence of correlation happens at a zero time lag, without any indication of a delay. Although the significance is estimated to be ∼2.5σ using Monte Carlo simulations, this suggestion is interesting in the context of previous results as well as the newly available X-ray polarization measurements. First, we stress that this is the third time that an indication of X-ray versus UV anticorrelation is reported for Mrk 421 (Aleksić et al. 2015a; MAGIC Collaboration 2021), and each previous indication shows a similar anticorrelation trend over approximately monthly timescales. Secondly, the direct implication of an anticorrelation is a physical connection between the X-ray, UV and optical emitting regions. While the IXPE results strongly suggest that those regions are not co-spatial, the anticorrelation further supports a scenario in which particles are first accelerated close to a shock front and then advect (and cool) toward a broader region in the jet and dominate the observed UV and optical emission.

A possible scenario explaining the anticorrelation is a long-term evolution of the acceleration efficiency while the electron injection luminosity stays roughly constant. In this configuration, a decrease in the acceleration efficiency would increase the relative proportion of lower-energy electrons and shift the synchrotron SED toward lower frequencies (as suggested by the data), while keeping the amplitude of the SED peak at a

roughly similar level. This scenario is thus expected to generate an increase in the UV and optical flux (rising edge of the synchrotron component) and a decrease in the X-ray flux (falling edge of the synchrotron component).

Angelakis et al. (2016) find an indication of anticorrelation between the optical polarization degree and the synchrotron peak frequencies, ν_p, for a sample of BL Lac objects. This behavior was qualitatively explained by the fact that, in the case of BL Lac objects with lower ν_p (such as LSPs), the synchrotron peak is close to the optical band, which is emitted by freshly accelerated electrons near the shock. For HSPs, the optical range is farther from ν_p and thus comprises emission radiated by electrons that had time to advect away. It is downstream from the shock, where the level of magnetic field disorder increases, thus reducing the observed optical polarization degree. In the case where the anticorrelation between the UV and X-rays described above is caused by a shift in ν_p toward lower frequencies, one would thus expect a simultaneous rise in the optical polarization degree over time, with a value approaching 1 in the X-rays. Consistently, the period during which we report an indication of anticorrelation is accompanied by an increase in the optical polarization degree (see Sect. 4.3). The higher optical polarization degree would also explain the relatively high ratio between the optical/IR and X-ray polarization degree throughout the IXPE 2 and IXPE 3 epochs (which are within the time range where a hint of UV versus X-ray anticorrelation is reported).

Alternatively, the rise in the optical polarization degree during the UV versus X-ray anticorrelation time range may be caused by a progressive increase in the relative dominance of a few emitting zones radiating the optical and UV flux. Indeed, in the case where the optical flux receives contributions from many regions with different magnetic field configurations, the polarization degree would decrease.

Acknowledgements. The MAGIC Collaboration would like to thank the Instituto de Astrofísica de Canarias for the excellent working conditions at the Observatorio del Roque de los Muchachos in La Palma. The financial support of the German BMBF, MPG and HGF; the Italian INFN and INAF; the Swiss National Fund SNF; the grants PID2019-104114RB-C31, PID2019-104114RB-C32, PID2019-104114RB-C33, PID2019-105510GB-C31, PID2019-107847RB-C41, PID2019-107847RB-C42, PID2019-107847RB-C44, PID2019-107988GB-C22 funded by the Spanish MCIN/AEI/10.13039/501100011033; the Indian Department of Atomic Energy; the Japanese ICRR, the University of Tokyo, JSPS, and MEXT; the Bulgarian Ministry of Education and Science, National RI Roadmap Project DO1-400/18.12.2020 and the Academy of Finland grant nr. 320045 is gratefully acknowledged. This work was also been supported by Centros de Excelencia "Severo Ochoa" y Unidades "María de Maeztu" program of the Spanish MCIN/AEI/ 10.13039/501100011033 (SEV-2016-0588, CEX2019-000920-S, CEX2019-000918-M, CEX2021-001131-S, MDM-2015-0509-18-2) and by the CERCA institution of the Generalitat de Catalunya; by the Croatian Science Foundation (HrZZ) Project IP-2016-06-9782 and the University of Rijeka Project uniri-prirod-18-48; by the Deutsche Forschungsgemeinschaft (SFB1491 and SFB876); the Polish Ministry of Education and Science grant No. 2021/WK/08; and by the Brazilian MCTIC, CNPq and FAPERJ. A.A.E. and D.P. acknowledge support from the Deutsche Forschungsgemeinschaft (DFG; German Research Foundation) under Germany's Excellence Strategy EXC-2094–390783311. The Imaging X-ray Polarimetry Explorer (IXPE) is a joint US and Italian mission. The US contribution is supported by the National Aeronautics and Space Administration (NASA) and led and managed by its Marshall Space Flight Center (MSFC), with industry partner Ball Aerospace (contract NNM15AA18C). The Italian contribution is supported by the Italian Space Agency (Agenzia Spaziale Italiana, ASI) through contract ASI-OHBI-2017-12-I.0, agreements ASI-INAF-2017-12-H0 and ASI-INFN-2017.13-H0, and its Space Science Data Center (SSDC), and by the Istituto Nazionale di Astrofisica (INAF) and the Istituto Nazionale di Fisica Nucleare (INFN) in Italy. This research used data products provided by the IXPE Team (MSFC, SSDC, INAF, and INFN) and distributed with additional software tools by the High-Energy Astrophysics Science Archive Research Center (HEASARC), at NASA Goddard Space Flight Center (GSFC). The *Fermi* LAT Collaboration acknowledges generous ongoing support from a number of agencies and institutes that have supported both the development and the operation of the LAT as well as scientific data analysis. These include the National Aeronautics and Space Administration and the Department of Energy in the United States, the Commissariat à l'Énergie Atomique and the Centre National de la Recherche Scientifique/Institut National de Physique Nucléaire et de Physique des Particules in France, the Agenzia Spaziale Italiana and the Istituto Nazionale di Fisica Nucleare in Italy, the Ministry of Education, Culture, Sports, Science and Technology (MEXT), High Energy Accelerator Research Organization (KEK) and Japan Aerospace Exploration Agency (JAXA) in Japan, and the K. A. Wallenberg Foundation, the Swedish Research Council and the Swedish National Space Board in Sweden. Additional support for science analysis during the operations phase is gratefully acknowledged from the Istituto Nazionale di Astrofisica in Italy and the Centre National d'Études Spatiales in France. This work performed in part under DOE Contract DE-AC02-76SF00515. The IAA-CSIC group acknowledges financial support from the Spanish "Ministerio de Ciencia e Innovación" (MCIN/AEI/ 10.13039/501100011033) through the Center of Excellence Severo Ochoa award for the Instituto de Astrofísica de Andalucía-CSIC (CEX2021-001131-S), and through grants PID2019-107847RB-C44 and PID2022-139117NB-C44. The POLAMI observations were carried out at the IRAM 30 m Telescope. IRAM is supported by INSU/CNRS (France), MPG (Germany), and IGN (Spain). Some of the data are based on observations collected at the Observatorio de Sierra Nevada, owned and operated by the Instituto de Astrofísica de Andalucía (IAA-CSIC). Further data are based on observations collected at the Centro Astronómico Hispano en Andalucía (CAHA), operated jointly by Junta de Andalucía and Consejo Superior de Investigaciones Científicas (IAA-CSIC). Some of the data reported here are based on observations made with the Nordic Optical Telescope, owned in collaboration with the University of Turku and Aarhus University, and operated jointly by Aarhus University, the University of Turku, and the University of Oslo, representing Denmark, Finland, and Norway, the University of Iceland and Stockholm University at the Observatorio del Roque de los Muchachos, La Palma, Spain, of the Instituto de Astrofisica de Canarias. E. L. was supported by Academy of Finland projects 317636 and 320045. The data presented here were obtained (in part) with ALFOSC, which is provided by the Instituto de Astrofisica de Andalucia (IAA) under a joint agreement with the University of Copenhagen and NOT. We acknowledge funding to support our NOT observations from the Finnish Centre for Astronomy with ESO (FINCA), University of Turku, Finland (Academy of Finland grant nr 306531). We are grateful to Vittorio Braga, Matteo Monelli, and Manuel Sänchez Benavente for performing the observations at the Nordic Optical Telescope. The research at Boston University was supported in part by National Science Foundation grant AST-2108622, NASA Fermi Guest Investigator grants 80NSSC21K1917 and 80NSSC22K1571, and NASA Swift Guest Investigator grant 80NSSC22K0537. This research was conducted in part using the Mimir instrument, jointly developed at Boston University and Lowell Observatory and supported by NASA, NSF, and the W.M. Keck Foundation. We thank D. Clemens for guidance in the analysis of the Mimir data. This research has made use of data from the RoboPUol program, a collaboration between Caltech, the University of Crete, IA-FORTH, IUCAA, the MPIfR, and the Nicolaus Copernicus University, which was conducted at Skinakas Observatory in Crete, Greece. D.B., S.K., R.S., N.M., acknowledge support from the European Research Council (ERC) under the European Unions Horizon 2020 research and innovation program under grant agreement No. 771282. C.C. acknowledges support from the European Research Council (ERC) under the HORIZON ERC Grants 2021 program under grant agreement No. 101040021. This study used observations conducted with the 1.8 m Perkins Telescope (PTO) in Arizona (USA), which is owned and operated by Boston University. This work was supported by NSF grant AST-2109127. We acknowledge the use of public data from the Swift data archive. Based on observations obtained with *XMM-Newton*, an ESA science mission with instruments and contributions directly funded by ESA Member States and NASA. This publication makes use of data obtained at Metsähovi Radio Observatory, operated by Aalto University in Finland. The Submillimetre Array is a joint project between the Smithsonian Astrophysical Observatory and the Academia Sinica Institute of Astronomy and Astrophysics and is funded by the Smithsonian Institution and the Academia Sinica. Mauna Kea, the location of the SMA, is a culturally important site for the indigenous Hawaiian people; we are privileged to study the cosmos from its summit. This work was supported by JST, the establishment of university fellowships toward the creation of science and technology innovation, Grant Number JPMJFS2129. This work was supported by Japan Society for the Promotion of Science (JSPS) KAKENHI Grant Numbers JP21H01137. This work was also partially supported by the Optical and Near-Infrared Astronomy Inter-University Cooperation Program from the Ministry of Education, Culture, Sports, Science and Technology (MEXT) of Japan. We are grateful to the observation and operating members of the Kanata Telescope. S.K. acknowledges support from

the European Research Council (ERC) under the European Unions Horizon 2020 research and innovation program under grant agreement No. 771282.

References

Abdo, A. A., Ackermann, M., Agudo, I., et al. 2010a, ApJ, 716, 30
Abdo, A. A., Ackermann, M., Ajello, M., et al. 2010b, Nature, 463, 919
Abdo, A. A., Ackermann, M., Ajello, M., et al. 2011, ApJ, 736, 131
Abdollahi, S., Acero, F., Ackermann, M., et al. 2020, ApJS, 247, 33
Abeysekara, A. U., Benbow, W., Bird, R., et al. 2020, ApJ, 890, 97
Acciari, V. A., Arlen, T., Aune, T., et al. 2014, Astropart. Phys., 54, 1
Acciari, V. A., Ansoldi, S., Antonelli, L. A., et al. 2020, ApJS, 248, 29
Acciari, V. A., Ansoldi, S., Antonelli, L. A., et al. 2021, MNRAS, 504, 1427
Ackermann, M., Ajello, M., Albert, A., et al. 2012, ApJS, 203, 4
Agudo, I., Thum, C., Molina, S. N., et al. 2018a, MNRAS, 474, 1427
Agudo, I., Thum, C., Ramakrishnan, V., et al. 2018b, MNRAS, 473, 1850
Ahnen, M. L., Ansoldi, S., Antonelli, L. A., et al. 2017a, A&A, 603, A29
Ahnen, M. L., Ansoldi, S., Antonelli, L. A., et al. 2017b, Astropart. Phys., 94, 29
Albert, J., Aliu, E., Anderhub, H., et al. 2007, Nucl. Instrum. Methods Phys. Res. A, 583, 494
Aleksić, J., Ansoldi, S., Antonelli, L. A., et al. 2015a, A&A, 576, A126
Aleksić, J., Ansoldi, S., Antonelli, L. A., et al. 2015b, A&A, 578, A22
Aleksić, J., Ansoldi, S., Antonelli, L. A., et al. 2016, Astropart. Phys., 72, 76
Angelakis, E., Hovatta, T., Blinov, D., et al. 2016, MNRAS, 463, 3365
Arbet-Engels, A., Baack, D., Balbo, M., et al. 2021, A&A, 647, A88
Arnaud, K. A. 1996, ASP Conf. Ser., 101, 17
Atwood, W. B., Abdo, A. A., Ackermann, M., et al. 2009, ApJ, 697, 1071
Ballet, J., Burnett, T. H., Digel, S. W., & Lott, B. 2020, arXiv e-prints [arXiv:2005.11208]
Baloković, M., Paneque, D., Madejski, G., et al. 2016, ApJ, 819, 156
Baring, M. G., Böttcher, M., & Summerlin, E. J. 2017, MNRAS, 464, 4875
Blandford, R., & Eichler, D. 1987, Phys. Rep., 154, 1
Böttcher, M., Reimer, A., Sweeney, K., & Prakash, A. 2013, ApJ, 768, 54
Breeveld, A. A., Landsman, W., Holland, S. T., et al. 2011, Am. Inst. Phys. Conf. Ser., 1358, 373
Brinkmann, W., Papadakis, I. E., den Herder, J. W. A., & Haberl, F. 2003, A&A, 402, 929
Burrows, D. N., Hill, J. E., Nousek, J. A., et al. 2005, Space Sci. Rev., 120, 165
Cerruti, M., Zech, A., Boisson, C., & Inoue, S. 2015, MNRAS, 448, 910
Chandra, S., Zhang, H., Kushwaha, P., et al. 2015, ApJ, 809, 130
de la Calle Pérez, I., Álvarez Crespo, N., Racero, E., & Rouco, A. 2021, A&A, 655, A48
Di Gesu, L., Donnarumma, I., Tavecchio, F., et al. 2022, ApJ, 938, L7
Di Gesu, L., Marshall, H. L., Ehlert, S. R., et al. 2023, Nat. Astron., 7, 1245
Domínguez, A., Primack, J. R., Rosario, D. J., et al. 2011, MNRAS, 410, 2556
Drury, L. O. 1983, Rep. Prog. Phys., 46, 973
Edelson, R. A., & Krolik, J. H. 1988, ApJ, 333, 646
Emmanoulopoulos, D., McHardy, I. M., & Papadakis, I. E. 2013, MNRAS, 433, 907
Fitzpatrick, E. L. 1999, PASP, 111, 63
Gabriel, C., Denby, M., Fyfe, D. J., et al. 2004, ASP Conf. Ser., 314, 759
Ghisellini, G., Tavecchio, F., & Chiaberge, M. 2005, A&A, 432, 401
Ghisellini, G., Righi, C., Costamante, L., & Tavecchio, F. 2017, MNRAS, 469, 255
Gupta, A. C., Gaur, H., Wiita, P. J., et al. 2019, AJ, 157, 95
Harrison, F. A., Craig, W. W., Christensen, F. E., et al. 2013, ApJ, 770, 103
HI4PI Collaboration (Ben Bekhti, N., et al.) 2016, A&A, 594, A116
Ho, P. T. P., Moran, J. M., & Lo, K. Y. 2004, ApJ, 616, L1
Horan, D., Acciari, V. A., Bradbury, S. M., et al. 2009, ApJ, 695, 596
Jansen, F., Lumb, D., Altieri, B., et al. 2001, A&A, 365, L1
King, O. G., Blinov, D., Ramaprakash, A. N., et al. 2014, MNRAS, 442, 1706
Kirk, J. G., Rieger, F. M., & Mastichiadis, A. 1998, A&A, 333, 452
Kirk, J. G., Guthmann, A. W., Gallant, Y. A., & Achterberg, A. 2000, ApJ, 542, 235
Kusunose, M., Takahara, F., & Li, H. 2000, ApJ, 536, 299
Larionov, V. M., Jorstad, S. G., Marscher, A. P., et al. 2013, ApJ, 768, 40
Liodakis, I., Marscher, A. P., Agudo, I., et al. 2022, Nature, 611, 677
Lumb, D. H., Warwick, R. S., Page, M., & De Luca, A. 2002, A&A, 389, 93
Madejski, G. M., Sikora, M., Jaffe, T., et al. 1999, ApJ, 521, 145
Madsen, K. K., Harrison, F. A., Markwardt, C. B., et al. 2015, ApJS, 220, 8
Madsen, K. K., Beardmore, A. P., Forster, K., et al. 2017, AJ, 153, 2
MAGIC Collaboration (Ahnen, M. L., et al.) 2018, A&A, 619, A45
MAGIC Collaboration (Acciari, V. A., et al.) 2020, A&A, 635, A158
MAGIC Collaboration (Acciari, V. A., et al.) 2021, A&A, 655, A89
Mannheim, K. 1993, A&A, 269, 67
Maraschi, L., Ghisellini, G., & Celotti, A. 1992, ApJ, 397, L5
Marrone, D. P., & Rao, R. 2008, Proc. SPIE, 7020, 70202B
Marscher, A. P., & Gear, W. K. 1985, ApJ, 298, 114
Marscher, A. P., & Jorstad, S. G. 2021, Galaxies, 9, 27
Marscher, A. P., Jorstad, S. G., D'Arcangelo, F. D., et al. 2008, Nature, 452, 966
Mattox, J. R., Bertsch, D. L., Chiang, J., et al. 1996, ApJ, 461, 396
Nilsson, K., Pasanen, M., Takalo, L. O., et al. 2007, A&A, 475, 199
Padovani, P., Alexander, D. M., Assef, R. J., et al. 2017, A&A Rev., 25, 2
Patel, S. R., Shukla, A., Chitnis, V. R., et al. 2018, A&A, 611, A44
Poutanen, J., Zdziarski, A. A., & Ibragimov, A. 2008, MNRAS, 389, 1427
Primiani, R. A., Young, K. H., Young, A., et al. 2016, J. Astron. Instrum., 5, 1641006a
Ramaprakash, A. N., Rajarshi, C. V., Das, H. K., et al. 2019, MNRAS, 485, 2355
Ravasio, M., Tagliaferri, G., Ghisellini, G., & Tavecchio, F. 2004, A&A, 424, 841
Roming, P. W. A., Kennedy, T. E., Mason, K. O., et al. 2005, Space Sci. Rev., 120, 95
Rybicki, G. B., & Lightman, A. P. 1979, Radiative Processes in Astrophysics (New York: Wiley)
Schlafly, E. F., & Finkbeiner, D. P. 2011, ApJ, 737, 103
Schlegel, D. J., Finkbeiner, D. P., & Davis, M. 1998, ApJ, 500, 525
Strüder, L., Briel, U., Dennerl, K., et al. 2001, A&A, 365, L18
Tavecchio, F. 2021, Galaxies, 9, 37
Tavecchio, F., Maraschi, L., & Ghisellini, G. 1998, ApJ, 509, 608
Teraesranta, H., Tornikoski, M., Mujunen, A., et al. 1998, A&AS, 132, 305
Thum, C., Wiesemeyer, H., Paubert, G., Navarro, S., & Morris, D. 2008, PASP, 120, 777
Turner, M. J. L., Abbey, A., Arnaud, M., et al. 2001, A&A, 365, L27
Urry, C. M., & Padovani, P. 1995, PASP, 107, 803
Vaughan, S., Edelson, R., Warwick, R. S., & Uttley, P. 2003, MNRAS, 345, 1271
Weaver, Z. R., Jorstad, S. G., Marscher, A. P., et al. 2022, ApJS, 260, 12
Weisskopf, M. 2022, AAS/High Energy Astrophysics Division, 54, 301.01
Zanin, R., Carmona, E., Sitarek, J., et al. 2013, Int. Cosmic Ray Conf., 33, 2937
Zhang, H., & Böttcher, M. 2013, ApJ, 774, 18
Zhang, Y. H., Treves, A., Celotti, A., et al. 2002, ApJ, 572, 762

[1] Japanese MAGIC Group: Institute for Cosmic Ray Research (ICRR), The University of Tokyo, Kashiwa 277-8582, Chiba, Japan
[2] ETH Zürich, 8093 Zürich, Switzerland
[3] Instituto de Astrofísica de Canarias and Dpto. de Astrofísica, Universidad de La Laguna, 38200 La Laguna, Tenerife, Spain
[4] Instituto de Astrofísica de Andalucía-CSIC, Glorieta de la Astronomía s/n, 18008 Granada, Spain
[5] National Institute for Astrophysics (INAF), 00136 Rome, Italy
[6] Università di Udine and INFN Trieste, 33100 Udine, Italy
[7] Max-Planck-Institut für Physik, 85748 Garching, Germany
[8] Università di Padova and INFN, 35131 Padova, Italy
[9] Institut de Física d'Altes Energies (IFAE), The Barcelona Institute of Science and Technology (BIST), 08193 Bellaterra (Barcelona), Spain
[10] Croatian MAGIC Group: University of Zagreb, Faculty of Electrical Engineering and Computing (FER), 10000 Zagreb, Croatia
[11] IPARCOS Institute and EMFTEL Department, Universidad Complutense de Madrid, 28040 Madrid, Spain
[12] Centro Brasileiro de Pesquisas Físicas (CBPF), 22290-180 URCA Rio de Janeiro (RJ), Brazil
[13] University of Lodz, Faculty of Physics and Applied Informatics, Department of Astrophysics, 90-236 Lodz, Poland
[14] Centro de Investigaciones Energéticas, Medioambientales y Tecnológicas, 28040 Madrid, Spain
[15] Departament de Física, and CERES-IEEC, Universitat Autònoma de Barcelona, 08193 Bellaterra, Spain
[16] Università di Pisa and INFN Pisa, 56126 Pisa, Italy
[17] Universitat de Barcelona, ICCUB, IEEC-UB, 08028 Barcelona, Spain
[18] Department for Physics and Technology, University of Bergen, Norway
[19] INFN MAGIC Group: INFN Sezione di Torino and Università degli Studi di Torino, 10125 Torino, Italy
[20] INFN MAGIC Group: INFN Sezione di Catania and Dipartimento di Fisica e Astronomia, University of Catania, 95123 Catania, Italy

[21] INFN MAGIC Group: INFN Sezione di Bari and Dipartimento Interateneo di Fisica dell'Università e del Politecnico di Bari, 70125 Bari, Italy
[22] Croatian MAGIC Group: University of Rijeka, Faculty of Physics, 51000 Rijeka, Croatia
[23] Technische Universität Dortmund, 44221 Dortmund, Germany
[24] University of Geneva, Chemin d'Ecogia 16, 1290 Versoix, Switzerland
[25] Japanese MAGIC Group: Physics Program, Graduate School of Advanced Science and Engineering, Hiroshima University, 739-8526 Hiroshima, Japan
[26] Deutsches Elektronen-Synchrotron (DESY), 15738 Zeuthen, Germany
[27] Armenian MAGIC Group: ICRANet-Armenia, 0019 Yerevan, Armenia
[28] Croatian MAGIC Group: University of Split, Faculty of Electrical Engineering, Mechanical Engineering and Naval Architecture (FESB), 21000 Split, Croatia
[29] Universität Würzburg, 97074 Würzburg, Germany
[30] Croatian MAGIC Group: Josip Juraj Strossmayer University of Osijek, Department of Physics, 31000 Osijek, Croatia
[31] Finnish MAGIC Group: Finnish Centre for Astronomy with ESO, University of Turku, 20014 Turku, Finland
[32] Japanese MAGIC Group: Department of Physics, Tokai University, Hiratsuka 259-1292, Kanagawa, Japan
[33] Università di Siena and INFN Pisa, 53100 Siena, Italy
[34] Saha Institute of Nuclear Physics, A CI of Homi Bhabha National Institute, Kolkata 700064, West Bengal, India
[35] Inst. for Nucl. Research and Nucl. Energy, Bulgarian Academy of Sciences, 1784 Sofia, Bulgaria
[36] Japanese MAGIC Group: Department of Physics, Yamagata University, Yamagata 990-8560, Japan
[37] Finnish MAGIC Group: Space Physics and Astronomy Research Unit, University of Oulu, 90014 Oulu, Finland
[38] Japanese MAGIC Group: Chiba University, ICEHAP, 263-8522 Chiba, Japan
[39] Japanese MAGIC Group: Institute for Space-Earth Environmental Research and Kobayashi-Maskawa Institute for the Origin of Particles and the Universe, Nagoya University, 464-6801 Nagoya, Japan
[40] Japanese MAGIC Group: Department of Physics, Kyoto University, 606-8502 Kyoto, Japan
[41] INFN MAGIC Group: INFN Sezione di Perugia, 06123 Perugia, Italy
[42] INFN MAGIC Group: INFN Roma Tor Vergata, 00133 Roma, Italy
[43] Japanese MAGIC Group: Department of Physics, Konan University, Kobe, Hyogo 658-8501, Japan
[44] Also at International Center for Relativistic Astrophysics (ICRA), Rome, Italy
[45] Now at Institute for Astro- and Particle Physics, University of Innsbruck, 6020 Innsbruck, Austria
[46] Also at Port d'Informació Científica (PIC), 08193 Bellaterra, (Barcelona), Spain
[47] Also at Institute for Astro- and Particle Physics, University of Innsbruck, 6020 Innsbruck, Austria
[48] Also at Department of Physics, University of Oslo, Norway
[49] Also at Dipartimento di Fisica, Università di Trieste, 34127 Trieste, Italy
[50] Max-Planck-Institut für Physik, 85748 Garching, Germany
[51] Also at INAF, 35122 Padova, Italy
[52] Japanese MAGIC Group: Institute for Cosmic Ray Research (ICRR), The University of Tokyo, Kashiwa 277-8582, Chiba, Japan
[53] INAF Istituto di Radioastronomia, Via P. Gobetti 101, 40129 Bologna, Italy
[54] Finnish Centre for Astronomy with ESO, 20014 University of Turku, Finland
[55] Institute for Astrophysical Research, Boston University, 725 Commonwealth Avenue, Boston, MA 02215, USA
[56] ASI – Agenzia Spaziale Italiana, Via del Politecnico snc, 00133 Roma, Italy
[57] INAF Istituto di Astrofisica e Planetologia Spaziali, Via del Fosso del Cavaliere 100, 00133 Roma, Italy
[58] Dipartimento di Fisica, Università degli Studi di Roma "La Sapienza", Piazzale Aldo Moro 5, 00185 Roma, Italy
[59] Dipartimento di Fisica, Università degli Studi di Roma "Tor Vergata", Via della Ricerca Scientifica 1, 00133 Roma, Italy
[60] Space Science Data Center, Agenzia Spaziale Italiana, Via del Politecnico snc, 00133 Roma, Italy
[61] INAF Osservatorio Astronomico di Roma, Via Frascati 33, 00078 Monte Porzio Catone (RM), Italy
[62] Quasar Science Resource S.L. for the European Space Agency (ESA), European Space Astronomy Centre (ESAC), Camino Bajo del Castillo s/n, 28692 Villanueva de la Cañada, Madrid, Spain
[63] Foundation for Research and Technology – IESL Hellas, Greece
[64] Institute of Astrophysics, Voutes 7110, Heraklion, Greece
[65] Department of Physics, University of Crete, 70013 Heraklion, Greece
[66] Institute of Astrophysics, Foundation for Research and Technology-Hellas, 71110 Heraklion, Greece
[67] Owens Valley Radio Observatory, California Institute of Technology, MC 249-17, Pasadena, CA 91125, USA
[68] Department of Physics, Tokyo Institute of Technology, 2-12-1 Ookayama, Meguro-ku, Tokyo 152-8551, Japan
[69] Department of Physics, Graduate School of Advanced Science and Engineering, Hiroshima University Kagamiyama, 1-3-1 Higashi-Hiroshima, Hiroshima 739-8526, Japan
[70] Hiroshima Astrophysical Science Center, Hiroshima University, 1-3-1 Kagamiyama Higashi-Hiroshima, Hiroshima 739-8526, Japan
[71] Core Research for Energetic Universe (Core-U), Hiroshima University, 1-3-1 Kagamiyama, Higashi-Hiroshima, Hiroshima 739-8526, Japan
[72] Planetary Exploration Research Center, Chiba Institute of Technology, 2-17-1 Tsudanuma, Narashino, Chiba 275-0016, Japan
[73] Institut de Radioastronomie Millimétrique, Avenida Divina Pastora, 7, Local 20, 18012 Granada, Spain
[74] Max-Planck-Institut für Radioastronomie, Auf dem Hügel 69, 53121 Bonn, Germany
[75] Aalto University Metsähovi Radio Observatory, Metsähovintie 114, 02540 Kylmälä, Finland
[76] Aalto University Department of Electronics and Nanoengineering, PO Box 15500, 00076 Aalto, Finland
[77] Center for Astrophysics | Harvard & Smithsonian, 60 Garden Street, Cambridge, MA 02138, USA
[78] NASA Marshall Space Flight Center, Huntsville, AL 35812, USA
[79] Also affiliated at Physik Department, Technische Universität München, James-Franck-Str. 1, 85748 Garching, Germany

Appendix A: *XMM-Newton* fine-binned light curves

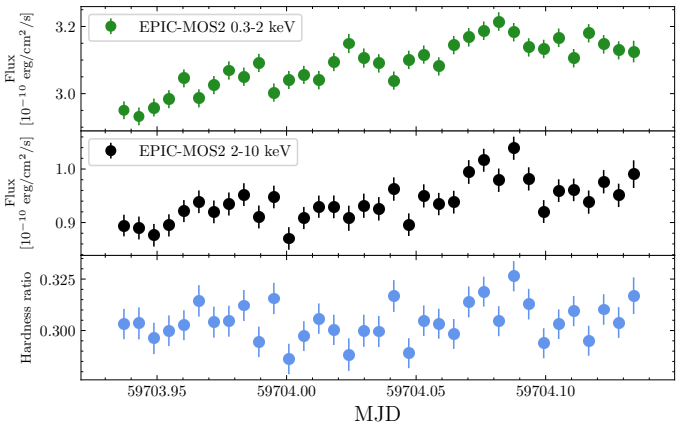

Fig. A.1. *XMM-Newton* light curve from the EPIC-MOS2 camera in the 0.3-2 keV and 2-10 keV bands during the IXPE 1 epoch. The lower panel is the ratio between the 2-10 keV and 0.3-2 keV fluxes.

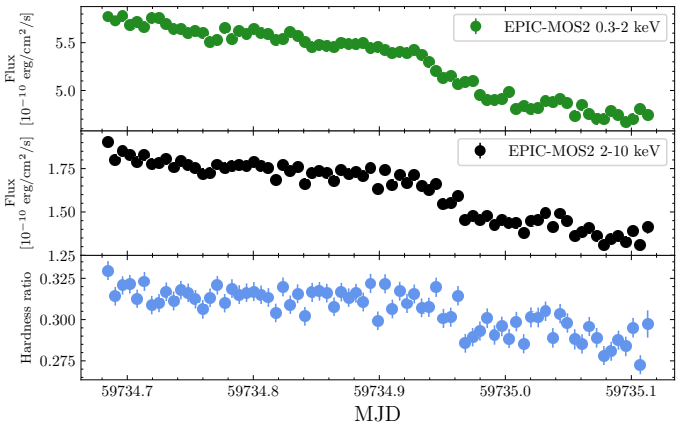

Fig. A.2. *XMM-Newton* light curve from the EPIC-MOS2 camera in the 0.3-2 keV and 2-10 keV bands during the IXPE 2 epoch. The lower panel is the ratio between the 2-10 keV and 0.3-2 keV fluxes.

In this section, we present the fine-binned light curves from both of the *XMM-Newton* exposures analyzed in this work. The fluxes were computed using the EPIC-MOS2 camera (which has the largest exposure time among the operating instruments on board *XMM-Newton*) in the 0.3-2 keV and 2-10 keV bands using a temporal binning of 500 s. The SAS task `epiclccorr` was used to produce background-subtracted source count rates corrected for the inefficiencies of the instrument (vignetting, chip gaps, point spread functions, etc.) and time corrections (dead time, GTIs...). The count rates were then converted to energy fluxes (i.e., in erg/cm^2/s units) assuming the best-fit log parabola model over the entire exposure. The light curve for the IXPE 1 and the IXPE 2 epochs are shown in Fig. A.1 and Fig. A.2, respectively. The bottom panel present the ratio between the 2-10 keV and the 0.3-2 keV fluxes.

Appendix B: VHE versus 0.2-3 keV DCF analysis

This section presents the results of the DCF analysis between the VHE fluxes and the 0.3-2 keV band from *Swift*-XRT. Figures B.1 and B.2 show the DCF when the VHE flux is computed in the 0.2-1 TeV and $>$ 1 TeV ranges, respectively. The dashed lines

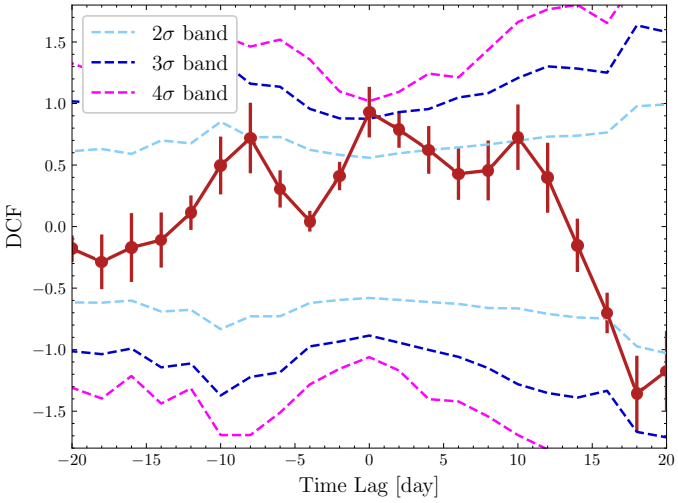

Fig. B.1. DCF computed for the MAGIC 0.2−1 TeV and *Swift*-XRT 0.3-2 keV light curves between MJD 59700 (May 1, 2022) and MJD 59740 (June 10, 2022) with a time binning of 2 days. The red points are the obtained DCF values and their uncertainties. The light blue, dark blue and pink dashed lines show the 2σ, 3σ and 4σ significance bands, respectively (see the main text for more details).

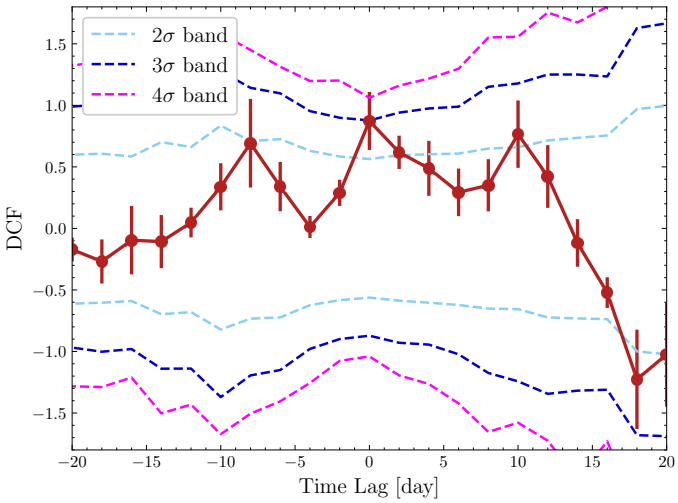

Fig. B.2. DCF computed for the MAGIC $>$ 1 TeV and *Swift*-XRT 0.3-2 keV light curves between MJD 59700 (May 1, 2022) and MJD 59740 (June 10, 2022) with a time binning of 2 days. The red points are the obtained DCF values and their uncertainties. The light blue, dark blue and pink dashed lines show the 2σ, 3σ and 4σ significance bands, respectively (see the main text for more details).

are the confidence bands based on Monte Carlo simulations (see Sect. 4 for more details).

Appendix C: UV versus X-ray correlation

This section presents the results of the DCF analysis between the X-ray and the UV fluxes in the *Swift*-UVOT W1 filter. Figures C.1 and C.2 show the DCF when the X-ray flux is computed in the 0.3-2 keV and 2-10 keV ranges, respectively, using data between MJD 59710 and MJD 59740 (i.e., corresponding to the second part of the MWL campaign presented in this work; May 11, 2022, to June 10, 2022). The dashed lines are the confidence bands based on Monte Carlo simulations (see Sect. 4 for more details about the procedure). In Fig. C.3 and Fig. C.4, we

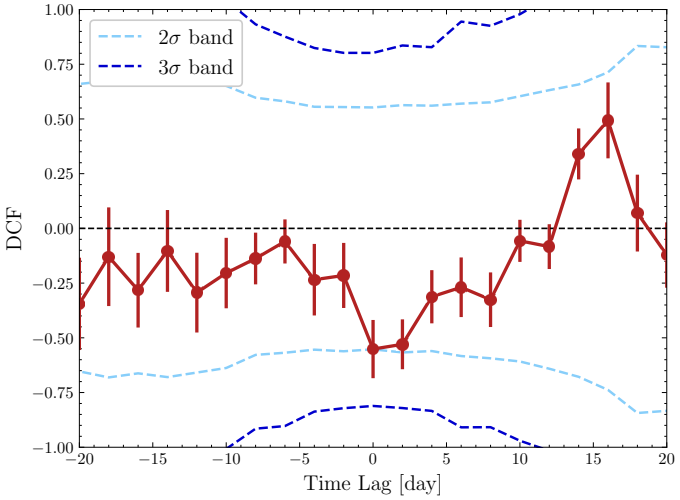

Fig. C.1. DCF computed for the *Swift*-UVOT W1 and *Swift*-XRT 0.3-2 keV light curves over the second part of the MWL campaign, between MJD 59710 (May 11, 2022) and MJD 59760 (June 30, 2022), with a time-lag binning of 2 days. The red points are the obtained DCF values and their uncertainties. The light blue and dark blue dashed lines show the 2σ and 3σ significance bands, respectively (see the main text for more details).

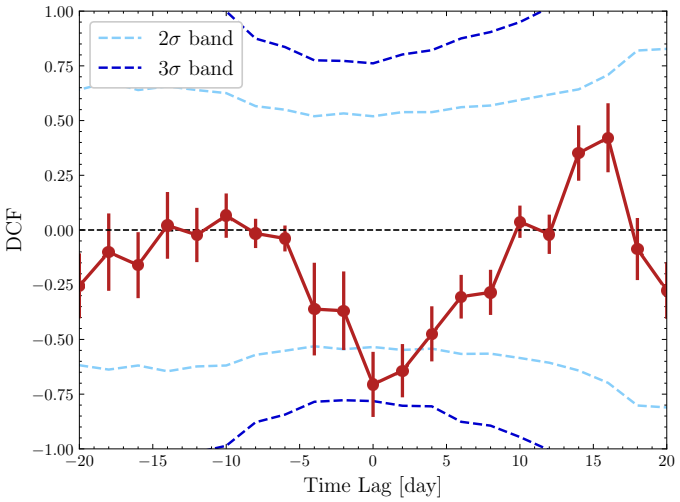

Fig. C.2. DCF computed for the *Swift*-UVOT W1 and *Swift*-XRT 2-10 keV light curves over the second part of the MWL campaign, between MJD 59710 (May 11, 2022) and MJD 59760 (June 30, 2022), with a time-lag binning of 2 days. The red points are the obtained DCF values and their uncertainties. The light blue and dark blue dashed lines show the 2σ and 3σ significance bands, respectively (see the main text for more details).

display the results after repeating the exercise when data from the entire MWL campaign were included (i.e., from MJD 59695 to MJD 59740; April 26, 2022, to June 10, 2022).

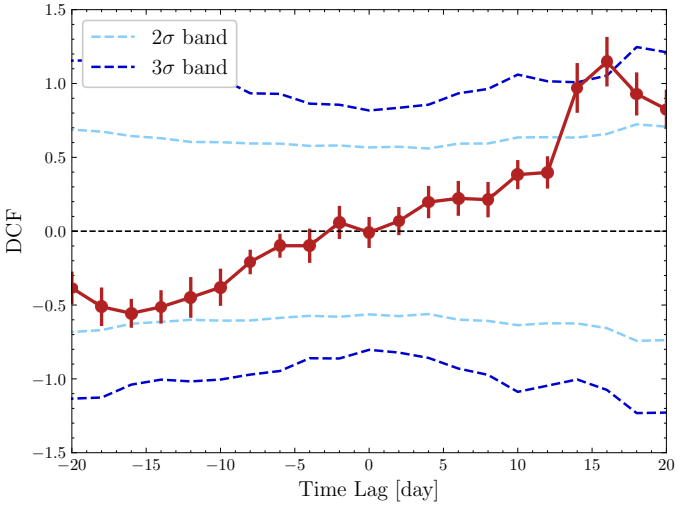

Fig. C.3. DCF computed for the *Swift*-UVOT W1 and *Swift*-XRT 0.3-2 keV light curves over the full MWL campaign, between MJD 59695 (April 26, 2022) and MJD 59760 (June 30, 2022), with a time-lag binning of 2 days. The red points are the obtained DCF values and their uncertainties. The light blue and dark blue dashed lines show the 2σ and 3σ significance bands, respectively (see the main text for more details).

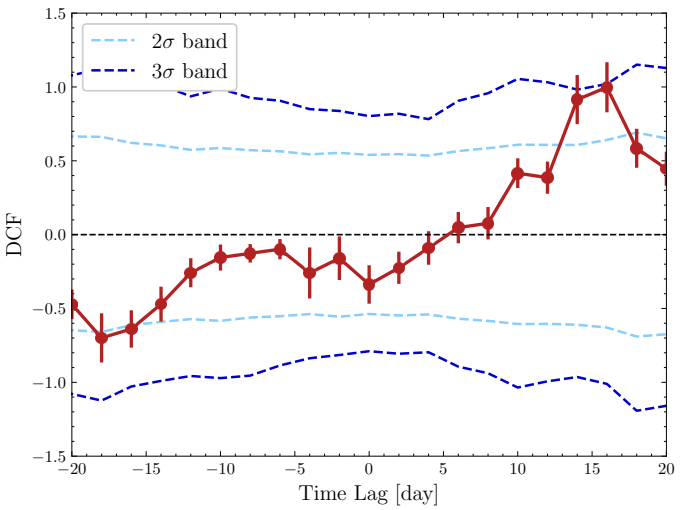

Fig. C.4. DCF computed for the *Swift*-UVOT W1 and *Swift*-XRT 2-10 keV light curves over the full campaign, between MJD 59695 (April 26, 2022) to MJD 59760 (June 30, 2022), with a time-lag binning of 2 days. The red points are the obtained DCF values and their uncertainties. The light blue and dark blue dashed lines show the 2σ and 3σ significance bands, respectively (see the main text for more details).

Appendix D: Modeling of the X-ray and VHE spectra during the IXPE epochs

Table D.1. Model parameters of the one-zone SSC model applied to the IXPE 1 epoch.

Parameter	Value
B' [G]	4.2×10^{-2}
R' [cm]	2×10^{16}
δ	30
U'_e [erg cm^{-3}]	9.5×10^{-4}
n_1	2.0
n_2	4.5
γ'_{min}	10^3
γ'_{br}	1.1×10^5
γ'_{max}	0.9×10^6
U'_B [erg cm^{-3}]	0.7×10^{-4}
$U'_{synch,avail}$ [erg cm^{-3}]	0.3×10^{-4}

Notes. See the text in Appendix D for a description of the parameters.

Table D.2. Model parameters of the one-zone SSC model applied to the IXPE 2 epoch.

Parameter	Value
B' [G]	3.8×10^{-2}
R' [cm]	2×10^{16}
δ	30
U'_e [erg cm^{-3}]	11.0×10^{-4}
n_1	2.0
n_2	4.7
γ'_{min}	10^3
γ'_{br}	1.8×10^5
γ'_{max}	1.1×10^6
U'_B [erg cm^{-3}]	0.6×10^{-4}
$U'_{synch,avail}$ [erg cm^{-3}]	0.3×10^{-4}

Notes. See the text in Appendix D for a description of the parameters.

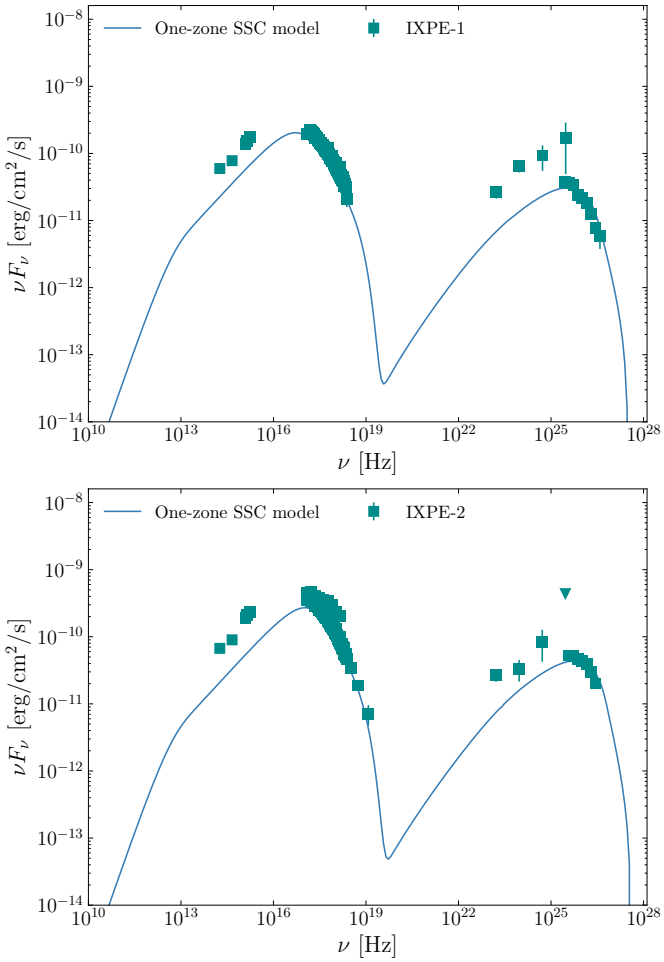

Fig. D.1. Results of a one-zone SSC model applied to the IXPE 1 (top panel) and IXPE 2 (bottom panel) epochs in order to constrain the physical parameters of the X-ray and VHE emitting region. The data are plotted with cyan markers, and the model is shown as a solid blue line. The obtained modeling parameters are listed in Tables D.1 and D.2. The reader is referred to Appendix D for more details on the model.

In Sect. 5 we present calculations of the ratio between the cooling and acceleration timescales of X-ray-emitting electrons during the hysteresis loops that we detect in the *NuSTAR* data during IXPE 3. The ratio between the two timescales is then used to estimate the *gyro-factor* ξ. For simplification, only synchrotron cooling is considered, and IC cooling is neglected. In this section, we address the validity of this assumption.

Following the notation of Tavecchio et al. (1998), the IC cooling timescale is estimated as

$$t'_{cool,IC} = \frac{3 m_e c}{4 \sigma_T U'_{synch,avail} \gamma}, \quad \text{(D.1)}$$

where $U'_{synch,avail}$ is the available target photon density for IC process (below the Klein-Nishina limit; see Eq. 20 in Tavecchio et al. 1998) within the emitting zone. The estimation of $t'_{cool,IC}$ requires the knowledge of $U'_{synch,avail}$, which we extracted with a simple modeling of the SED by considering a one-zone SSC model (Maraschi et al. 1992; Madejski et al. 1999). For this exercise, we aim at describing the X-ray and VHE spectra only for the following reasons. First, a description of the radio-to-VHE data would require a more complex modeling that takes into account the energy stratification of the jet implied by the broadband polarization data. This effort lies beyond the scope of this work. Secondly, describing the X-ray and VHE spectra in a one-zone SSC approach is motivated by the tight X-ray versus VHE correlation at zero time lag. Since only IXPE 1 and IXPE 2 have simultaneous X-ray and VHE data we are forced to focus on those two epochs to constrain physical parameters of the source during IXPE 3, where the hysteresis loops actually happened. This represents a caveat for the following analysis since the source parameters may have evolved between the different epochs.

We first fixed the radius of the emitting region to $R' = 2{\times}10^{16}$ cm. This was derived from the constraints using causality arguments, $R' \lesssim \delta \cdot c \cdot t_{var,obs}$ (Tavecchio et al. 1998), where $t_{var,obs}$ is the observed variability timescale and δ the Doppler factor, which we fixed to 30 (a typical value adopted for Mrk 421 in previous modeling; see, e.g. Tavecchio et al. 1998; Baloković et al. 2016; MAGIC Collaboration 2021). Here, we set $t_{var,obs} = 7$ hr, which is the halving and/or doubling time that we measured in the *NuSTAR* band. We modeled the electron distribution with a

broken power law,

$$\frac{dN'}{d\gamma'}(\gamma') = \begin{cases} N'_0\,\gamma'^{\,-n_1}, & \gamma'_{min} < \gamma' < \gamma'_{br} \\ N'_0\,\gamma'^{\,n_2-n_1}_{br}\,\gamma'^{-n_2}, & \gamma'_{br} < \gamma' < \gamma'_{max}, \end{cases} \tag{D.2}$$

where N'_0 is a normalization constant. γ'_{min}, γ'_{br}, and γ'_{max} are defined as the minimum, break, and maximum Lorentz factor, respectively. Differently from n_2, n_1 cannot be constrained by the X-ray and VHE data, so we fix $n_1 = 2.0$, close to the predictions of shock acceleration (Kirk et al. 2000). The overall electron energy density is given by U'_e. The resulting models are shown in Fig. D.1, and exhibit a reasonable description of the X-ray and VHE data. We list in Table D.1 and Table D.2 the obtained parameters. The optical/UV and MeV-GeV data are purposely under-predicted. In fact, the energy stratification of jet suggested by the polarization data strongly implies that optical, UV and MeV-GeV fluxes receive a significant contribution from broader and separate regions than the X-ray and VHE one. Hence, our one-zone modeling does not intend to describe the entire SED.

The modeling yields $U'_{synch,avail} < U'_B$ in both epochs. From Eq. D.1 and Eq. 5, one thus concludes that IC cooling timescale is longer than the synchrotron cooling timescale. Only considering synchrotron cooling is thus a reasonable simplification to assess the cooling dynamics of the electrons during the hysteresis loops that we report and discuss in Sects. 3.6 and 5.